

Forced Flow of Vapor Condensing Over a Horizontal Plate (Problem of Cess and Koh)* - Steady and Unsteady Solutions of the Full 2-D Problem

S. Kulkarni, A. Narain (Email: narain@mtu.edu), and S. Mitra

Department of Mechanical Engineering-Engineering Mechanics
Michigan Technological University
Houghton, MI 49931

Abstract

Accurate steady and unsteady numerical solutions of the full 2-D governing equations – that model the forced film condensation flow of saturated vapor over a semi-infinite horizontal plate (the problem of Cess [1] and Koh [2]) - are obtained over a range of flow parameters. The results presented here are used to better understand the limitations of the well-known similarity solutions given by Koh [2]. It is found that steady/quasi-steady film wise solution exists only if the inlet speed is above a certain threshold value. Above this threshold speed, steady/quasi-steady film condensation solutions exist and their film thickness variations are approximately the same as the similarity solution given by Koh [2]. However these steady solutions differ from the Koh solution [2] regarding pressure variations and associated effects in the leading part of the plate. Besides results based on the solutions of the full steady governing equations, this paper also presents unsteady solutions that characterize the steady solutions' attainability, stability (response to initial disturbances), and their response to ever-present minuscule noise on the condensing surface. For this shear driven flow, the paper finds that if the uniform vapor speed is above a threshold value, an unsteady solution that begins with any reasonable initial guess, is attracted in time, to a steady solution. This long time limiting solution is the same – within computational errors – as the solution of the steady problem. The reported unsteady solutions that yield the steady solution in the long time limit also yield “attraction rates” for non-linear stability analysis of the steady solutions. The attraction rates are found to diminish gradually with increasing distance from the leading edge and with decreasing inlet vapor speed. These steady solutions are generally found to be stable to initial disturbances on the interface as well as in any flow variable in the interior of the flow domain.

The results for low vapor speeds below the threshold value indicate that the unsteady solutions exhibit non-existence of any steady limit of film wise flow in the aft portion of the solution. Even when a steady solution exists, the flow attainability is also shown to be difficult (because of waviness and other sensitivities) at large downstream distances.

* Cess, R. D., 1960, “Laminar Film Condensation on a Flat Plate in the Absence of a Body Force,” *Zeitschrift für Angewandte Mathematik und Physik*, 11, pp. 426-433 /Koh, J. C. Y., 1962, “Film Condensation in a Forced-Convection Boundary-Layer Flow,” *International Journal of Heat and Mass Transfer*, Vol. 5, pp. 941-954.

Key-words: film condensation, phase-change heat transfer, two-phase flows, stability, instability, interfacial waves.

Nomenclature

C_p	Specific heat, J/(kg·K)
\mathcal{D}_{\max}	Displacement amplitude of waves on the condensing surface, m
f	Non-dimensional frequency f_p of bottom wall vibrations given by $1/T_b \equiv f_p \cdot Y_e / U_\infty$
f_p	Physical value of frequency of bottom wall vibrations, Hz
Fr	Froude number $U_\infty^2 / g Y_e$
Ja	Jakob number given by $C_{p1} \Delta T / h_{fg}$
h_{fg}	Latent heat, J/kg
k	Thermal conductivity, W/(m·K)
\dot{m}	Non-dimensional value of interfacial mass flux, $\dot{m} \equiv \dot{m} / (\rho_1 \cdot U_\infty)$
\dot{m}	Physical value of interfacial mass flux, kg/(m ² ·s)
n_i	Representative number of grid points in x direction for simulations
n_j	Representative number of grid points in y direction for simulations
p	Pressure, N/m ²
p_∞	Pressure far field, N/m ²
Pr_I	Prandtl number $\mu_1 C_{p1} / k_1$
Re_δ	Film Reynolds number, $4\rho_1 u_{1\text{avg}}(x) \Delta(x) / \mu_1$
T_w	Non-dimensional time period of condensing surface vibrations
\mathcal{T}	Temperature, K
U_∞^*	Lower threshold of vapor speed U_∞ given by simulations for film wise condensation, m/s
U_∞	Far upstream vapor speed, m/s
(u, v)	Values of x and y components of velocity, m/s

(u,v)	Non-dimensional values of u and v , $(u,v) \equiv (u/U_\infty, v/U_\infty)$
v_{\max}	Physical value of the amplitude of a standing velocity wave associated with condensing surface noise, m/s
We	Weber number, $\rho_l U_\infty^2 Y_e / \sigma$
x_e	Non-dimensional value of domain length, X_e/Y_e
χ^*	Distance from the leading edge beyond which pressure gradient in liquid or vapor domain is nearly equal to zero, m
x^*	Non-dimensional value of χ^* , χ^*/Y_e
X_e	Physical value of domain length (distance from leading edge BC in Fig.1), m
x_e	Non-dimensional value of domain length, X_e/Y_e
(x, y, t)	Non-dimensional values of $(x, y, t) \equiv (x/Y_e, y/Y_e, (t \cdot U_\infty/Y_e))$ in the computational and problem formulation context.
Y_e	Characteristics length (OA in Fig.1), m
ΔT	Temperature difference between the vapor and the condensing-surface, °C
φ	Rate of energy dissipation inside a flow domain, W

Greek Symbols

π_l	Non-dimensional pressure, $p_l/(\rho_l \cdot U_\infty^2)$
θ	Non-dimensional temperature, $T/\Delta T$
ρ	Density, kg/m ³
μ	Viscosity, Pa-s
Δ	Physical value of condensate film thickness, m
δ	Non-dimensional value of condensate thickness, Δ/Y_e
ν	Kinematic viscosity μ/ρ , m ² /s

σ	Surface tension, N/m
λ	Non-dimensional wave-length for the bottom wall vibrations ($\lambda = \lambda_p/Y_e$)
λ_p	Physical/dimensional value of wavelength for the bottom wall vibrations, m
λ_o	Non-dimensional wave-length for the initial disturbance $\delta'(x, 0)$ on the interface
δ'	Non-dimensional value of disturbance on the interface

Subscripts

I	It takes a value of 1 for liquid phase and 2 for vapor phase
s	Saturation condition
w	Condensing surface

Superscripts

i	Value of a variable at an interface location
---	----------------------------------------------

1. Introduction

1.1 The Cess [1] and Koh [2] Problem and Related Similarity Solutions

The problem studied by Cess [1] and Koh [2] deals with forced flow of saturated vapor (with a uniform upstream speed U_∞) that approaches a semi-infinite horizontal plate and starts experiencing film-wise condensation over the plate (see Fig. 1). The central interest of this paper is to solve the steady and unsteady governing equations for the full two dimensional version of this problem, compare the steady solutions with the relevant classical similarity solutions offered by Cess [1] and Koh [2], and to improve our understanding of the feasibility of the film wise condensation assumption underlying the Cess [1] and Koh [2] solutions. The results of Koh [2] have been pivotal to the studies that rely on (e.g. Rose [3]) or use (e.g. Balasubramaniam et. al

[4]) this solution to predict or estimate the features of shear driven external condensing flows. The ordinary differential equations associated with the solution of Koh [2], which are numerically solved, result from a boundary layer and constant pressure approximation of an assumed film-wise condensation behavior and a “similarity” solution formulation of the resulting model equations. This solution’s approach is very similar to other similarity solutions (Sparrow and Gregg [5], Koh et. al [6]) for gravity-driven condensing flows that are well-cited in the literature. One reason why this similarity solution for the shear driven condensate case ([2]) has not been experimentally verified is, perhaps, significant differences exist between shear driven and gravity driven flows with regard to ease of attainment of film wise or annular condensation and another reason is the difficulty in implementing a suitable experiment that meets the requirements of the theory ([1], [2]). This is in contrast with the similarity solutions (e.g. Sparrow and Gregg [5] and Koh et al. [6]) for film wise condensation over a plate under conditions of gravity-driven condensate motion. The gravity driven cases’ similarity solutions are in good agreement with the Nusselt solution [7] and, also, known to be experimentally feasible and in reasonable agreement with related experiments [8]. With regard to ease of achieving film wise or annular condensation, similar differences are known to exist between gravity driven and shear driven internal condensing flows. The experiments involving gravity driven internal condensing flows inside a vertical tube (see [9], [10], etc.) or large hydraulic diameter slightly inclined (downward) channels demonstrate easy attainment of a rather robust quasi-steady wavy annular (or film condensation) flows but annular or film wise shear driven internal condensing flows in mm to μm -scale horizontal tubes and channels are more difficult to achieve and show ([11]-[14]) more complex vapor-liquid morphologies (such as steady or intermittent injection annular, mist, slug/plug, bubbly, etc.).

1.2 Steady and Unsteady Results Presented in this Paper

The computationally obtained steady solutions of the problem studied by Cess [1] and Koh [2] and their comparison with the well-known analytical results of Koh [2] have been discussed in this paper. It is shown here that, for a certain range of vapor speeds and vapor-to-wall temperature differences, Koh's analytical solution [2] of this external condensing flow problem agrees well with the reported computational solution's steady film thickness predictions. However the reported simulations differ from the Koh solution [2] in pressure and associated variables' variation near the leading edge of the plate. While the analytical solution of Koh [2] assumes that the pressure stays constant even in the interior of the flow, the steady solutions presented in this paper show that there are significant pressure variations near the leading edge part of the plate and though the resulting pressure differences are miniscule in value relative to the far field pressure p_∞ , they are very important for determining the dynamics of the flow and in determining the feasibility of maintaining film wise condensation at low vapor speeds. It is found that the leading edge pressure gradients become large as the vapor speed U_∞ becomes sufficiently small.

The unsteady solutions reported in this paper help assess attainability of the steady solutions. This is done here by looking at limiting solutions (as $t \rightarrow \infty$) of the unsteady problem obtained for different initial guesses. Additionally, important assessments of stability through unsteady response (to initial disturbances as well as to ever present bottom wall noises) of these flows are obtained and discussed. The effort to obtain and analyze unsteady solutions results in introduction and quantification of the following features of the steady solutions: (i) "attraction rate" values that measure the attainability of the steady solutions from different initial guesses,

(ii) response of the steady solutions to initial disturbances, and (iii) noise-sensitivity of the steady solutions to ever-present minuscule noise and, as a result, expected waviness levels on the steady solutions.

For the range of vapor speeds (0.2 m/s -20 m/s) considered for investigation of film wise condensation of typical non-metallic vapors (R113, FC-72, etc.), when an arbitrary initial guess (at $t = 0$) is used to obtain an unsteady solution in the idealized case of no condensing surface vibrations (no matter how minuscule), it is shown that the unsteady solutions tend to a smooth wave free long term steady solution. The limiting steady solution, when obtained this way as opposed to obtaining it as a steady solution of the steady governing equations, is termed a steady “attractor.” This unsteady attraction process is studied and “attraction rates” to the limiting steady solution are defined. Though the reported “attraction rates” associated with attainability of a steady solution may appear to be a new idea, it is related to the well known idea of “decay rates” in linearized stability analyses that assume exponential time evolution of initial disturbances. Thus increased monotonic (i.e. non-oscillatory) “attraction rates” reported here correlate with the idea of stronger “decay rates” (i.e. larger, real, and negative coefficients multiplying time in the exponential decay assumption in linear stability analyses). That is large “attraction rates” mean both attainability and stronger stability of the steady solution. The “attraction rates” are used here because, in the present non-linear context, they are both more general and computationally easier to obtain than “decay rates” in the linear context. It is found that this “attraction rate” when plotted as a function of time for any given point on the steady solution (which is close to Koh solution [2] – at least as far as steady film thickness values are concerned) may, in general, depend on the steady solution of the system (that is the underlying partial differential equations under no-noise conditions) as well as the starting initial conditions.

However we show here that a proper segment of the time-history associated with the rate of change of film thickness yields a definition of “attraction rate” which is more or less independent of the choice of initial guess. This properly chosen measure of “attraction rate” is shown to diminish with increasing distance from the leading edge and also with decreasing speed U_∞ . As a result, it is found that the assumed film wise steady condensation is difficult to achieve at very low free stream speeds and, for free stream speeds that are sufficiently large, attainment difficulty is predicted for large downstream distances.

For example, unsteady results find that at low vapor speeds ($U_\infty < U_\infty^* \approx 0.2$ m/s for the case discussed here), a long term steady limit is not reached and hence a film wise steady solution or a steady “attractor” does not exist. This result is further supported by the fact that the steady “attractor” (for $U_\infty > 0.2$ m/s in the example considered here) exhibits an approach to near zero mechanical energy availability for viscous dissipation in the interior of any chosen control volume.

For sufficiently fast vapor speeds, since the “attraction rate” diminishes with downstream distance, one expects sensitivity to the effects of: transverse gravity (see [9] for similar effects for condensation inside a horizontal channel), to unintended variations in the far field uniform pressure p_∞ , and to ever present minuscule noise on the condensing surface. Considering limitations imposed by our computational approach and the scope of the paper, this paper limits itself to demonstrating increasing downstream waviness associated with persistent but minuscule condensing surface noise. It is shown that when an arbitrary initial guess (at $t = 0$) is used to obtain an unsteady solution (for $t > 0$) in the presence of minuscule noise on the condensing surface (defined later in the paper through a representative Fourier component), the underlying long term solution’s diminishing attraction rates with distance cause the noise induced interfacial

waves to grow with the distance from the leading edge. A measure of spatial growth as well as its growth rate with distance is reported in this paper.

1.3 Trustworthiness of the Employed Computational Tool

The computational tool employed to solve the Koh problem [2] in this paper has been successfully used to solve internal as well as external condensing flow problems reported in [15]-[20]. The steady and unsteady simulation results and stability results for the classical Nusselt problem [7] by the tools employed in this paper have been already reported elsewhere in Phan and Narain [16]. The agreement of steady computational results in [16] with the Nusselt solution [7] as well as successful comparison of computational results in [15] - [20] for internal condensing flows with relevant semi-analytical ([9], [15]) and experimental results ([9], [15]) further strengthen the confidence in the results reported here.

2. Governing Equations and Formulation for the Computational Problem

The liquid and vapor phases in the flow (e.g., see Fig. 1) are denoted by a subscript I: I = 1 for liquid and I = 2 for vapor. As shown in Fig.1, the far upstream speed of the forced vapor flow is a uniform U_∞ . The fluid properties (density ρ , viscosity μ , specific heat C_p , and thermal conductivity k) with subscript “I” are assumed to take their representative constant values for each phase (I = 1 or 2). Let T_I be the temperature field (K), p_I be the pressure field (N/m²), $T_s(p)$ be the saturation temperature of the vapor (K) as a function of local pressure p , Δ be the film thickness (m), \dot{m} be the local interfacial mass flux (kg/(s·m²)), $T_w(x)$ be a *known* temperature variation (here, often, $T_w(x) = \text{constant} = T_w(0) < T_s(p)$) of the cooled bottom plate (K), and $\mathbf{v}_I = u_I \hat{\mathbf{e}}_x + v_I \hat{\mathbf{e}}_y$ be the velocity field (m/s). It is assumed here that $\Delta T \equiv T_s(p_\infty) - T_w(0)$ is always

sufficiently large to allow film condensation at all χ , including the $\chi \sim 0$ zone. For common metallic condensing surfaces and non-metallic (refrigerant) vapors, if ΔT is larger than 1-2°C and other surface-energy conditions are supportive, annular/stratified or film condensation can be assumed/realized and conditions for its attainment can be theoretically/experimentally assessed.

As shown in Fig. 1, instead of the original infinite domain ($\chi \geq 0$ and $y \geq 0$), solutions for this problem are to be computationally obtained over a finite domain ($0 \leq \chi \leq X_e$ and $0 \leq y \leq Y_e$). For convenience, the characteristic length for this problem is chosen to be Y_e , where Y_e can be chosen to be a known numerical multiple of the well known physical value of steady film thickness for an altogether different problem – the one associated with a vertical inclination of the plate (gravity driven condensate) and for $U_\infty = 0$ - viz. the Nusselt problem (see [7], [16]). That is, $Y_e \equiv c_1 \cdot \Delta_N(X_e)$, where $c_1 = 47$ for most of the cases considered here and $\Delta_N(X_e)$ is the Nusselt film thickness at $\chi = X_e$. An equivalent alternative is $Y_e \equiv (c_2 \cdot \mu_l) / (\rho_l \cdot h_{fg})^{0.5}$, where $c_2 = 1.133 \times 10^5$ for most of the cases considered here. These choices make Y_e an *a priori* known number that is sufficiently large to capture all the relevant vapor flow domain of interest here. Though other choices of intrinsic characteristic length Y_e are also possible (e.g. $Y_e = \mu_l / (\rho_l \cdot U_\infty)$ or $Y_e = \mu_l^{3/4} k_l^{1/4} \Delta T'^{-1/2} C_{p1}^{-3/4} \rho_l^{-1}$), the earlier two choices suffice here. Furthermore, as discussed in section 5, either of the two choices of Y_e is *a posteriori* verified to be effective by showing that the numerically obtained values of the flows' physical variables are independent of different choices of the number for Y_e . The above choice of Y_e for characteristic length and U_∞ for characteristic speed are used for defining the non-dimensional variables whose computationally obtained values are reported in this paper. As needed, these values can easily be related to the results obtained from other commonly used choices of characteristic length and speed. Let g_y be gravitational acceleration acting along y axis (gravity along x direction is zero

for this horizontal flow), p_∞ be the pressure of the far field vapor at $y \geq Y_e$, $\Delta T \equiv T_s(p_\infty) - T_w(0)$ be the representative controlling temperature difference between the vapor and the bottom plate, and h_{fg} be the heat of vaporization at saturation temperature $T_s(p)$. With t representing the physical time, a new list of fundamental non-dimensional variables is introduced through the following definitions:

$$\begin{aligned} \{x, y, \delta, u_1, \dot{m}\} &\equiv \left\{ \frac{x}{Y_e}, \frac{y}{Y_e}, \frac{\Delta}{Y_e}, \frac{u_1}{U_\infty}, \frac{\dot{m}}{\rho_l U_\infty} \right\}, \\ \{v_1, \theta_1, \pi_1, t\} &\equiv \left\{ \frac{v_1}{U_\infty}, \frac{T_1}{\Delta T}, \frac{p_1 - p_\infty}{\rho_l U_\infty^2}, \frac{t}{(Y_e/U_\infty)} \right\}. \end{aligned} \quad (1)$$

In what follows, all governing equations are presented in their more general unsteady forms.

Interior Equations

The non-dimensional differential forms of mass, momentum (x and y components) and energy equations for flow in the interior of either of the phases are well-known and are given in (A.1) - (A.4) of the Appendix. The simplified forms that are used in obtaining the Koh formulation ([2]) and its solution are given by (A.1) and (A.6) of the Appendix.

Interface Conditions

The nearly exact *physical variables form* of general interface conditions (Delhay [22]) for condensing flows, with some approximations, are used here and, in the form used here, they are given in Appendix Eqs. (A.1) - (A.9) of Narain et al. [18]. Utilizing a superscript, “i” for values of the flow variables at the interface given by $\mathcal{H} \equiv y - \Delta(x, t) = 0$, the *non-dimensional* forms of the interface conditions are given below in Eqs. (2) – (8). The Koh formulation [2] uses simplified versions of Eqs. (2) - (7) given below and they are, respectively, given as Eqs. (A.7)-(A.11) of the Appendix.

- The non-dimensional form of the requirement of continuity of tangential component of velocities (Eq. (A. 2) of [18]) becomes:

$$u_2^i = u_1^i - \delta_x (v_2^i - v_1^i), \quad (2)$$

where, $\delta_x \equiv \partial\delta/\partial x$.

- The non-dimensional form of the normal component of momentum balance at the interface (Eq. (A. 3) of [18]) becomes:

$$\pi_1^i = \frac{\rho_2}{\rho_1} \pi_2^i - \frac{1}{We} \left(\frac{\delta_{xx}}{[1+\delta_x^2]^{3/2}} \right) + \dot{m}^2 \left(\frac{\rho_1}{\rho_2} - 1 \right), \quad (3)$$

where $We^{-1} \equiv \sigma/\rho_1 U_\infty^2 Y_e$, and σ is the surface tension with $\sigma = \sigma(\mathcal{T})$ being a function of interfacial temperature \mathcal{T} . Though surface tension term is included here, over the range of computational investigations reported here, the presence or absence of the second and third terms on the right side of Eq. (3) were found to have none to negligible impact on simulation results reported here. Because of near constancy of interfacial saturation temperature (as interfacial pressure variations are not strong enough to change it), and resulting absence of Marangoni effects (see Eq. (4) below), the surface tension variation effect also shows no qualitative impact on the unsteady solutions reported here.

- The tangential component of momentum balance at the interface (Eq. (A. 4) of [18]) becomes:

$$\left. \frac{\partial u_1}{\partial y} \right|_i = \frac{\mu_2}{\mu_1} \left. \frac{\partial u_2}{\partial y} \right|_i + [t], \quad (4)$$

The resulting term $[t]$ used here is defined by Eq. (A.5) of the Appendix.

- The non-dimensional forms \dot{m}_{LK} and \dot{m}_{VK} of the non-zero physical values of interfacial mass fluxes \dot{m}_{LK} and \dot{m}_{VK} (defined in Eq. (A.5) of [18]) impose kinematic constraints on the interfacial values of the liquid and vapor velocity fields and are given by:

$$\begin{aligned}\dot{m}_{LK} &\equiv \left[u_1^i (\partial\delta/\partial x) - (v_1^i - \partial\delta/\partial t) \right] / \sqrt{1 + (\partial\delta/\partial x)^2}, \text{ and} \\ \dot{m}_{VK} &\equiv (\rho_2/\rho_1) \left[u_2^i (\partial\delta/\partial x) - (v_2^i - \partial\delta/\partial t) \right] / \sqrt{1 + (\partial\delta/\partial x)^2}.\end{aligned}\quad (5)$$

- The non-dimensional form \dot{m}_{Energy} of the non-zero physical values of interfacial mass flux \dot{m}_{Energy} (as given by Eq. (A.6) of [18]) represents the constraint imposed on mass flux by the balance equation for the net energy transfer across the interface, and is given by:

$$\dot{m}_{Energy} \equiv Ja / (Re_1 Pr_1) \{ \partial\theta_1 / \partial n \big|_i - (k_2/k_1) \partial\theta_2 / \partial n \big|_i \}, \quad (6)$$

where $Ja \equiv C_{p1} \Delta T / \hat{h}_{fg}^0$ and $\hat{h}_{fg}^0 \equiv \hat{h}_{fg}(T_s(p_\infty)) \cong \hat{h}_{fg}(T_s(p_2))$.

- The interfacial mass balance requires that the net mass flux (in kg/m²/s) at a point on the interface, as given by Eq. (A.7) of [18], be single-valued regardless of which physical process is used to obtain it. The non-dimensional form of this requirement becomes:

$$\dot{m}_{LK} = \dot{m}_{VK} = \dot{m}_{Energy} \equiv \dot{m}. \quad (7)$$

It should be noted that negligible interfacial thermal resistance and equilibrium thermodynamics on either side of the interface are assumed to hold at all values of x downstream of the origin (i.e., second or third computational cell onwards). Hence, as in Koh solution [2] and as per discussions in the Appendix of [18] (see Eq. (A.8) of [18]), no non-equilibrium thermodynamic model for the interfacial mass-flux \dot{m} is needed to obtain a solution.

- The non-dimensional thermodynamic restriction on interfacial temperatures (as given by Eq. (A.8) in [18]) becomes:

$$\theta_1^i \equiv \theta_2^i = \mathcal{T}_s(p_2^i)/\Delta \mathcal{T} \equiv \theta_s(\pi_2^i). \quad (8)$$

Within the vapor domain, for any of the typical refrigerants (such as R113 considered here), typical changes in absolute pressure relative to the inlet pressure are small but sufficient to affect vapor motion, though, at the same time, they are too small to affect saturation temperature values even for the largest adverse pressure gradient zone in the leading edge. This allows the approximation $\theta_s(\pi_2^i) \equiv \theta_s(0)$ to be a valid one.

Boundary Conditions

Since the vapor flow is nearly uniform at locations at large y , appropriate boundary conditions are prescribed along lines OA ($\chi = 0$), AB ($y = Y_e$ or $y = 1$) and BC ($\chi = X_e$ or $x = x_e = X_e/Y_e$) in Fig. 1. Assuming onset of condensation at $\chi = 0$ (i.e. $\Delta(0, t) = 0$), the boundary conditions are:

Inlet: At the inlet $x = 0$, we have:

$$u_2(0, y, t) = U_\infty, \quad \partial v_2 / \partial x \Big|_{x=0} = 0 \text{ on OA in Fig. 1} \quad (9)$$

Pressure is not prescribed across the inlet boundary but is prescribed to be the far field pressure p_∞ at the top corner reference location (point A with $x = 0$ and $y = OA$ in Fig. 1) on the inlet boundary. Pressures within the entire domain, including the inlet values $p_2(0, y, t)$, are calculated as part of the solution of the problem being considered. However, outside and above the control volume, one expects the far field pressures to be: $p_2 - p_\infty \equiv (\rho_2 U_\infty^2) \cdot \pi_2(0, y, t) = 0$ for $y \geq OA$

(see Fig. 1) or $y \geq 1$. For temperature, one also iteratively imposes the condition $T_2(0, y, t) = T_{\text{sat}}(p_2(0, y, t))$ - which is, in principle, a non-constant prescription of vapor temperature at the inlet.

It should be noted that prescription of pressure at reference location (point A in Fig. 1) does not make inlet boundary condition one of pressure-inlet. It remains a boundary where x-component of vapor velocity u_2 is uniform but y-component of vapor velocity v_2 is given the requisite freedom through the condition $\partial v_2 / \partial x|_{x=0} = 0$.

Top: On the top boundary, where $y = OA$ (see Fig. 1) or $y = 1$, the pressure is p_∞ and shear stress is nearly zero. This leads to standard far field boundary modeling condition:

$$\pi_2(x, 1, t) = 0 \text{ and } \partial u_2 / \partial y|_{(x, 1, t)} = 0 \text{ on AB in Fig. 1} \quad (10)$$

The temperature at the top boundary is also considered to be one of saturated vapor, i. e. $T_2(x, Y_e, t) = T_{\text{sat}}(p_\infty)$. Therefore, according to Eq. (1), $\theta_2(x, 1, t) = T_{\text{sat}}(p_\infty) / \Delta T$. If the temperature at the top boundary is allowed some superheat (5-10 °C), a non-zero thickness for temperature boundary layer develops near the interface. For *saturated* vapor flow conditions considered here, this thermal boundary layer thickness is not present. Even if the boundary layer has non-zero thickness because of presence of vapor superheat, a non-zero superheat has no impact on the reported results for most vapors (we have computationally verified this and the physical reasons are discussed later).

Exit:

As far as exit condition is concerned, none is needed for temperature. For the Koh problem [2], and the steady solution, the exit pressure remains externally unspecified and, as a result, it remains close to the far field pressure p_∞ if the exit is sufficiently far from the inlet. This is not only the original assumption of Koh formulation [2] but is also the assumption for most

parabolic external flow problems (such as single phase flow over a flat plate, etc.). For this modeling, either of the two formulations [A] or [B] below is used.

[A] The pressure is prescribed to be the uniform steady pressure p_∞ (i.e. non dimensional pressure π_2 of zero) along some of the vapor phase at the exit section (along BD' in Fig. 1) that is close to the top boundary. Thus the best way to faithfully reproduce the above assumption for pressure at the exit, is

$$\pi_2(x_e, y, t) \approx 0 \text{ and } \frac{\partial v_2}{\partial x}|_{(x_e, y, t)} \cong 0 . \quad (11)$$

whenever x_e and y are sufficiently large (i.e., y is on D'B in Fig. 1) . For smaller y values (i.e., y on CD' in Fig. 1 where the point D' at $x = X_e$ can be taken to be any point that is sufficiently close to the interface), no boundary condition is prescribed except for the “outflow” boundary condition. The “outflow” condition is simply that the mass flow across CD' – which specifically includes the liquid portion $0 \leq y \leq \Delta(X_e, t)$ – is such that it satisfies the overall mass balance for a control volume formed by the bounding surfaces $x = 0$, $x = X_e$, $y = 0$, and $y = Y_e$.

[B] The pressure is left unspecified along the entire (or most) vapor phase at the exit section (along BC in Fig. 1). Because uniform pressure p_∞ is already prescribed along the top (AB in Fig. 1), only an “outflow” condition at the exit section is enforced to preserve an overall mass balance for the entire control volume (see OABC in Fig. 1). This formulation is adequate as the resulting computational solution obtained under this formulation also satisfies the requisite $\pi_2(x_e, y, t) \approx 0$ condition. This steady or unsteady solution obtained under [B] is found to be nearly identical (within computational convergence bounds) to the solution under [A] above. So, from here and henceforth, unless otherwise stated, this exit formulation [B] is used to closely follow the original intent of the Koh formulation [2] – that is to assume that the uniform far field

pressure ($= p_\infty$) condition holds for the exit section if it is sufficiently far from the inlet and, as a result, at these locations no significant adjustments in cross-sectional kinetic energy takes place.

Condensing Surface:

At the condensing surface ($y = 0$), we have:

$$u_1(x,0,t) = v_1(x,0,t) = 0 \text{ and } \theta_1(x,0,t) = \theta_w \equiv T_w/\Delta T. \quad (12)$$

Preliminary Remarks about the Steady Formulation and Solution:

For the steady problem, all variables are considered time independent and all time derivatives are dropped. The temperature variations in the vapor field were computed but the variations were found to be, as is well known, quite insignificant for zero (or small) superheat. Therefore, for all practical purposes, vapor can be assumed to be at uniform saturation temperature – i.e. $\theta_2(x,y,t) \cong \theta_s(0)$ at all locations in the vapor domain. This is reasonable because effects of superheat ΔT_{sup} (in the typical 5 - 10°C range) are verifiably negligible because of the typically small values of vapor Jakob number ($Ja_2 \equiv Cp_2 \cdot \Delta T_{\text{sup}} / h_{fg}$) and thermal conductivity ratio k_2/k_1 (see Eq. (6)) that are encountered for most non-metallic vapor flow conditions of interest here.

Preliminary Remarks about the Unsteady Formulation:

The governing equations and the interface conditions given above are valid under the *continuum* assumption and, therefore, they cannot model and incorporate various inter-molecular forces that are important in determining the time evolution of very thin (10 - 100 nm) condensate film thickness $\delta(x,t)$. As a result, for solving unsteady problems, $t = 0$ cannot be chosen to be the

time when saturated vapor first comes in contact with and condenses on the dry sub-cooled ($\mathcal{T}_w(x) < \mathcal{T}_s(p_\infty)$) horizontal condensing-surface. With the above modeling limitations, the strategy for obtaining unsteady solutions is to start at a time ($t = 0$) for which one either has a sufficiently thick *steady* solution of the *continuum* equations (where all the governing equations clearly apply) or one has *any* reasonable, but sufficiently thick, initial guess. Then, from there, one can obtain the unique large time ($t \rightarrow \infty$) smooth or wavy (steady/quasi-steady) condensate flow solution/behavior – if one exists - with the help of the unsteady *continuum* equations. The reported computational results verify the fact that the large times (or long term) unsteady solutions are independent of the choice of initial condition and thus represent (also see [9]) steady or unsteady features of the limiting steady solution for this flow.

Initial Conditions for the Unsteady Formulation:

In the context of the above discussion, if $\phi(x,y,t)$ is any variable (such as u_I , v_I , π_I , θ_I , etc.), the initial values of ϕ and film thickness $\delta(x,t)$ are given as:

$$\phi(x,y,0) = \phi_{\text{steady}}(x,y) \text{ or } \phi_{\text{initial-guess}}(x,y) \text{ and } \delta(x,0) = \delta_{\text{steady}}(x) \text{ or } \delta_{\text{initial-guess}}(x), \quad (13)$$

where $\phi_{\text{initial-guess}}$ and/or $\delta_{\text{initial-guess}}$ are reasonable initial guesses and ϕ_{steady} and/or δ_{steady} are the solutions of the governing equations obtained by dropping all time dependencies in Eqs. (2) - (12) above.

An inspection of all the non-dimensional governing equations, interface conditions, and boundary conditions reveals the fact that the computational solutions given here are affected by the following set of seven independent non-dimensional parameters:

$$\{\text{Re}_1, \text{Ja}, \text{Fr}_y^{-1}, \frac{\rho_2}{\rho_1}, \frac{\mu_2}{\mu_1}, \text{Pr}_1, \text{We}\}, \quad (14)$$

where $\text{Fr}_y^{-1} = U_\infty^2/g_y Y_e$ and $\text{Re}_1 \equiv \rho_1 U_\infty Y_e/\mu_1$. As we see later, for the downstream distances considered in this paper, the role of Fr_y^{-1} is insignificant. The role of surface tension, through We , is also found to be insignificant for cases considered here.

3. Koh's Formulation for a Similarity Solution of the Steady Problem

The formulation for this problem (see Cess [1] or Koh [2]) is posed by governing equations (A.1) and (A.6) of the Appendix along with the interface and boundary conditions given in (A.7)-(A.12) of the Appendix. The “similarity” formulation is sought after rewriting (A.1) and (A.6) following an introduction of certain assumed forms of velocity and temperature functions in terms of two new similarity variables (η for the liquid phase and ξ for the vapor phase) that replace x and y . These “new” similarity variables are defined as

$$\eta(x, y) \equiv y \sqrt{\frac{U_\infty}{v_1 x}} \quad , \quad \xi(x, y) \equiv (y - \Delta(x)) \sqrt{\frac{U_\infty}{v_2 x}} \quad (15)$$

The physical variables of velocity and temperature are sought as functions (viz. f_1, f_2, g_1 , and g_2) of the variables introduced above. The defining relations for these physical variables (see Koh [2]) are:

$$p_1(x, y) = p_\infty = \text{constant} \quad (\text{I} = 1 \text{ or } 2), \quad \Delta(x) \equiv \Delta_{\text{Koh}}(x) \equiv \eta_\delta \sqrt{\frac{v_1 x}{U_\infty}} \quad , \quad u_1(x, y) \equiv U_\infty f_1'(\eta) \quad (16)$$

$$u_2(x, y) \equiv U_\infty f_2'(\xi) \quad , \quad T_1(x, y) - T_w \equiv \Delta T \cdot g_1(\eta) \quad , \quad T_2(x, y) - T_w \equiv \Delta T \cdot g_2(\xi) \quad (17)$$

Eqs. (15) - (17) transform the governing equations (A.1), (A.6), and interface/boundary conditions (A.7)-(A.12) given in the Appendix for the Koh formulation [2], to (also see [2]) a set of ordinary differential equations (ODE) over the liquid ($0 \leq \eta \leq \eta_\delta$) and vapor ($0 \leq \xi < \infty$) domains with proper boundary conditions at $\eta = 0$, $\eta = \eta_\delta$, $\xi = 0$, and $\xi \rightarrow \infty$. This ODE formulation – unlike the formulation in section 2 – is *always* such that a unique steady solution exists and can be numerically obtained by a suitable method (e.g. fourth order Runge-Kutta method combined with a shooting technique that can satisfy all the boundary conditions). Thus, the steady Koh formulation (which is *always* well-posed and solvable for plates of large finite length) cannot, by itself, assess attainability issues for these solutions. The solution obtained by Koh's method, based on the results presented here, are found to represent a meaningful approximate solution, when a solution exists, either as a *steady* solution of the steady version of the formulation in section 2 or as the long term steady limit of the *unsteady* formulation in section 2.

4. Computational Approach

A detailed description of the 2-D steady/unsteady computational approach utilized in this paper is given in section 3 of Narain et al. [18]. A brief description of all essential features of computational approach is also available in section 3 of Liang et al. [19]. Since this paper investigates an external flow problem, unlike the internal flows discussed in [18] and [19], the imposition of the top and exit boundaries for this external flow is different from the internal flow situations but is the same as the one given by us in Phan and Narain [16] for the external flow Nusselt problem [7]. The difference is primarily another use of the earlier established ([14]) τ - p

method towards prescribing stress boundary-conditions – i.e., pressure (with τ = normal derivative of the tangential velocity component = 0) on the top (AB in Fig. 1) and side (BD' in Fig. 1) boundaries. The τ - p method was originally developed (see [18]) for prescribing τ (tangential velocity gradient in the normal direction) and p (pressure) at the interface.

5. Computational Results Obtained for Steady Solutions

5.1 Results Obtained for the Full Steady Problem and Comparison with Koh Solution [2]

Even though refrigerant R113's properties were used to run most of the computational simulations presented in this paper, similar results are expected, in principle, for any non-metallic pure vapor flowing over a flat plate.

The Koh formulation [2] discussed in section 3 is best represented by solution of the steady problem under unspecified exit conditions (see eq. (11)) as described in section 2. After establishing near equivalence of solutions obtained by imposing exit conditions under formulations [A] and [B] of section-2, the formulation [B] is used here to obtain the computational solutions of the steady problem and to discuss their comparisons with the corresponding Koh solutions [2]. For a representative R113 flow case, specified by sufficiently fast $U_\infty = 2$ m/s, $x_e = 45$, $\Delta T = 5^\circ$ C, and $g_y = 0$, the results obtained from steady solution are shown in Figs. 2-6. Figure 2 compares, for a representative case, non-dimensional film thickness values predicted by computational solution of the complete steady version of the formulation described in section 2 with the numerical solution of the Koh formulation [2] described in section 3.

It is seen that the computationally obtained values of film thickness are in good agreement with the classical similarity solution as the underlying boundary layer approximations for the Koh formulation [2] are approximately valid. For the case in Fig. 2, comparisons of vapor and liquid u-velocity profiles and liquid and vapor temperature profiles as obtained from the two different solution approaches were found to agree with each other (not shown here for brevity).

Thus film thickness, velocity profiles, and the temperature profiles from our simulations are in good agreement with Koh's approximate solution. This establishes that, for the ranges of vapor speeds investigated here, the solution obtained from Koh's similarity formulation (see summary in section 3) yields film thickness, velocity, and temperature profiles with reasonable accuracy (e.g., both the formulations yield, as expected, linear velocity and temperature profiles in the liquid domain for the laminar condensate flow).

For the case in Fig. 2, Fig. 3 shows the non-dimensional pressure variation $\pi_2(x, y)$ for $0 \leq x \leq 45$ in the vapor domain along the x direction at $y = 0.8$ (note that, for the corresponding case in Fig. 2, $\delta(x_e) < 0.8$ and, therefore, $y = 0.8$ is entirely in the vapor). The Koh formulation [2] in section 3 neglects the pressure gradient terms in the governing momentum equations but, as seen from Fig. 3, there is a zone $0 < x \leq x^*$ near the leading edge, up to which there exists a significant adverse pressure gradient that is needed to slow the vapor down by the amount that is consistent with the slow motion of the adjacent condensate and mass transfer across its interface. After this length x^* ($= \chi^*/Y_e$), pressure gradient $d\pi_2/dx$ reduces nearly to zero value and Koh's [2] assumption of uniform pressure is valid. The pressure gradient in this frontal zone ($0 < x \leq x^*$) is very significant in determining the vapor and condensate dynamics for this horizontal condensing flow problem. As the vapor speed reduces, this pressure gradient is found to increase. For the same case, the non-dimensional pressure profiles (values of $\pi_2(y)$ for $y \geq \delta(x)$)

and values of $\rho_1 \pi_1(y)/\rho_2$ for $0 \leq y \leq \delta(x)$ across the plate at different cross sections are shown in Fig. 4. The pressure discontinuities across the interface in Fig. 4 arise from the last two terms on the right side of Eq. (3) and are found to be inconsequential because of their smallness. The cross-sectional pressure rise seen in Fig. 4 over the same frontal part, is needed to provide the necessary centripetal acceleration for bending some of the streamlines (see Fig. 5) towards the condensate. As seen from Fig. 3, the pressure variations over the locations $x \geq x^*$ are insignificant as $\pi_2(x, y = 0.8) \approx 0$. In the computational results obtained from the formulation described in section 2, this bending of streamlines is assisted by pressure variations along and across the vapor domain as well as the variations in interfacial velocities (see, e.g., u_1^i variations in Fig. 6). Unlike this solution of the full formulation, in the similarity solution obtained from the formulation summarized in section 3, the pressure and interfacial velocity variations are not present and the bending of the streamline is kinematically enforced by an assumed constant value of pressure, constant value of interfacial velocity ($u_1^i \approx u_2^i$) independent of x , and condensate thickness values constrained by Eq. (16). Though, in the frontal portion of the plate, the computational solution of the full problem significantly differs in its pressure predictions from the Koh solution [2] obtained under the assumption of constant pressure, the two solutions differ by less than 1 % in the important heat transfer rate controlling values of film thickness variation. This agreement (within 1-2%) for film thickness variations was found to be valid over a range of flow parameters ($2 \cdot 10^5 \leq Re_x \leq 6 \cdot 10^7$, $0.02 \leq Ja \leq 0.12$, $0.0052 \leq (\rho_2/\rho_1) \leq 0.00526$, $0.020 \leq (\mu_2/\mu_1) \leq 0.0212$, $7 \leq Pr_1 \leq 7.5$) investigated by us.

The differences in the pressure fields cause the differences between the simulation and the Koh solution in the converged values of the vertical and horizontal component of condensate velocities at the interface viz. $v_1^i = v_1(x, \delta(x))$ (not shown) and in $u_1^i = u_1(x, \delta(x))$ shown in Fig.

6. Figure 6 shows a mismatch between the horizontal components of interfacial velocities as obtained by computational solution of the full steady problem and those obtained by the Koh similarity solution [2]. This mismatch occurs over a leading edge zone ($0 \leq x \leq x^*$) that is the same for which there is significant variation in vapor pressure field (see Fig. 3).

The streamline pattern (Fig. 5) obtained from computations has been compared with the streamline pattern (not shown) obtained from the Koh solution [2] for the same case. Both of the patterns were found to be very similar to each other. It is seen that the streamlines bend at the interface and that this bending reduces at the interface as one moves further downstream in x direction.

It is also found that, over the relatively short distances and vapor speeds considered in this paper, the transverse component of gravity insignificantly affects the film thickness values and velocity profiles of the steady solution. The transverse component of gravity does, however, affect the condensate pressure profiles in the y direction and we also know - from the results given [9] for internal condensing flows in horizontal channels – that transverse component of gravity does affect the flow at sufficiently long downstream distances once condensate thickness is “sufficiently” large. This version of our simulation tool for this external flow problem is not able to go far enough downstream to detect the phenomena we have observed, in [9], for internal flows in horizontal channels.

The above discussions for $U_\infty = 2$ m/s describe a region $0 \leq x \leq x^*$ (≈ 20) for which the pressure variations in the vapor phase (Figs. 3-4) and interfacial speed u_1^i (Fig. 6) differ from the Koh solution [2] and yet the film thickness variations in Fig. 2 are close to the Koh solution [2] for all $x > 2$ and not just $x > 20$. If U_∞ is reduced, it is found that the value of x^* decreases, film

thickness values increase, and the physical values of interfacial shear $S^i \approx \mu_1 (\partial u_1 / \partial y)^i$ also decrease as per Koh [2] predictions.

5.2 Numerical Accuracy and Regularities of the Computationally Obtained Solutions

The computational procedure for obtaining steady and unsteady solutions as described above, was verified for accuracy and consistency with regard to different choices of the number of grid points as well as different choices of the characteristic length Y_e appearing in Fig. 1 and in the definition of non-dimensional parameters listed in Eq. (14).

We only show here grid independence for the steady solution scheme employed here though similar grid independence has also been established for the reported unsteady solution scheme. In Fig. 7, film thickness variations for the same flow situation is computationally obtained for two different grids and two different choices of Y_e values. In Fig. 7, $Y_e = 0.004$ m is used for “Grid 1” and $Y_e = 0.008$ m is used for “Grid 2.” Furthermore, for “Grid 1” and “Grid 2,” the number of grid points represented by “ $n_i \times n_j$ ” values (see Narain et al. [18]) are respectively given as 30×50 and 35×70 . Although Fig. 7 only shows the nearly equal values of the two equivalent non-dimensional film thickness values, similar proximity of the two solutions was confirmed for velocity, temperature, and relative pressure profiles as well. From computational point of view, it should be observed that shear driven horizontal condensing flows, as opposed to gravity driven flows ([15] – [20]), require more iterations to converge.

5.3 Other Comments/Results

Since the computational cases deal with high vapor velocities ($U_\infty = 0.2 - 20$ m/s), it is natural to ask whether the Koh [2] assumption of *laminar* nature of the vapor flow holds for the near interface region. Since the near interface vapor flow is qualitatively similar to a boundary

layer flow with suction, it can be assumed that the transition to turbulence criteria for such boundary layer flows – as given by Eq. (17.10) of Schlichting [23] – will yield reasonable estimates for determining whether or not the vapor boundary layer flow in the Koh problem [2] is laminar or turbulent. The computationally obtained vapor boundary layer (momentum) thickness Δ_v values in the Koh solution as well as the values obtained from the computational solution was used to verify that Eq. (17.10) of [23], viz. $\rho_2 U_\infty \Delta_v(x) / \mu_2 \ll 70,000$, holds for all cases considered here. That is, these vapor flows, because of the suction effects, appear to be strongly laminar at all x locations considered here. However, such vapor-phase boundary-layer stability arguments based on vapor suction rates, may miss “stability” or “noise-sensitivity” of the associated condensate motion and this must be separately assessed in determining attainability and waviness of these flows.

6. Computational Results Obtained from Unsteady Solutions

6.1 Unsteady Simulation Results That Indicate the Domain and Attraction Rates of the Steady Solution

The unsteady computational solutions based investigations cover speeds U_∞ in a range of $0.2 \text{ m/s} < U_\infty < 20 \text{ m/s}$ (for the reported R-113 and similar vapors) and, for temperature difference $\Delta\mathcal{T}$, a range of $3 - 15^\circ\text{C}$ is covered. For this range, it is found that, if the unsteady solution was started at $t = 0$ from a reasonable initial guess for $\delta(x, 0)$, it would always seek a long-term time independent steady solution. The long-term ($t \rightarrow \infty$) steady solution of the unsteady governing equations is found to be computationally equal (within 3 to 5% of computational error) to the steady solution obtained by solving the steady governing equations.

This long-term ($t \rightarrow \infty$) steady solution obtained this way is termed an “attractor” because unsteady solutions starting at different initial guesses are attracted to it.

Though these solutions in Fig. 8 show the existence of a steady attractor, we observe that the phenomenon of attraction in Fig. 8 shows a different attraction rate to the steady solution at different downstream locations. The example shown in Fig. 8 is for R-113 vapor at $U_\infty = 1.7$ m/s and $\Delta T = 5^\circ\text{C}$. In Fig. 8, the unsteady solution is started at $t = 0$ with an initial guess of $\delta(x, 0)$ that is about 16% below the final attracting steady solution. A similar attracting behavior, though not shown here, exists if the initial guess was somewhat above the long term steady solution. It is seen from Fig. 8 that the attraction to the steady solution takes progressively longer times for locations that are farther and farther downstream of the inlet. The steady solution “attractor” in Fig. 8 is said to have a “strength” which diminishes with x . Here, by “strength,” one means the rate of steadily falling values of $\partial\Delta/\partial t$ as indicated by representative slopes of “ $\partial\Delta/\partial t$ vs. t ” curves for different values of x (these slopes are indicated by representative line segments AB, A'B', etc. in Fig. 9). As shown in Fig. 9, for the no-noise unsteady simulation results at $x = 0.12$ m, initial guess at any x has a delay time τ_{d1} over which the attraction speed $\partial\Delta/\partial t|_{\text{init}}$ does not change by much. Following this, over time duration τ_{eff} , there is a nearly constant representative deceleration rate $\left|\partial^2\Delta/\partial t^2\right|_{\text{Repl}(\text{no-noise})}$ (termed “attraction rates” and measured by the slopes of lines AB, A'B', etc.). This deceleration rate is needed to impede the attracting solution so it can reach a nearly steady ($\partial\Delta/\partial t \approx 0$) behavior over a subsequent time duration τ_{d2} .

Figure 10 shows “ $\partial\Delta/\partial t$ vs. t ” curves at $x = 30$ for three different vapor speeds. For all the speeds compared in Fig. 10, initially guessed $\delta(x, 0)$ values were approximately 16 % below their corresponding long-term steady solutions. In Fig. 10, it can be seen that the attraction rate

$\left| \partial^2 \Delta / \partial t^2 \right|_{\text{Repl}(\text{no-noise})}$ increases with increasing speed U_∞ and, through Fig. 9, it can be seen that the attraction rate decreases with downstream distance.

Figure 11 shows, at $x = 23$ and $U_\infty = 2$ m/s, “ $\partial \Delta / \partial t$ vs. t ” curves for different initial guesses. It is shown in this figure that the “attraction rates” obtained over the time segment τ_{Rep} are, indeed, more or less independent of initial conditions and thus represent the inherent character of the attracting steady solution. This justifies use of the magnitude of deceleration rates - given by the approximate slopes of the line segments AB, A'B', etc. - as “attraction rates.”

The above described trends were established for R113 flows for a range of vapor speeds $0.2 \text{ m/s} \leq U_\infty \leq 20 \text{ m/s}$, a range of temperature differences $3^\circ\text{C} \leq \Delta T \leq 15^\circ\text{C}$, and a range of domain lengths $0 \leq X_e \leq 0.4 \text{ m}$.

6.2 Stability of the “Steady Attractors”/Steady Solutions to Initial Interfacial Disturbances

The long term steady limit of the unsteady solution was found to exist (and be the same as the steady solution of the steady problem) for this horizontal external flow problem if the inlet speed U_∞ was above a certain threshold value (about 0.2 m/s for the example case discussed here). These solutions were tested for their response to the initial disturbances on the interface. Different vapor speeds ranging from 0.2 to 25 m/s were tested for interfacial disturbances of different non-dimensional wavelengths ranging from 5 to 30. Over the downstream distances investigated here, these external flows of vapor were found to be quite stable to the forward moving disturbances on the interface - whether or not transverse gravitational field was present. A representative example of this stable response to interfacial disturbances is shown in Fig. 12 where - even in the absence of the transverse component of gravity - the large initial disturbances

die out for the inlet vapor speed of $U_\infty = 3$ m/s and $\Delta T = 5^\circ\text{C}$. Computations show very stable response to these disturbances and all of these disturbances die out as the waves move downstream. The response to imposed disturbances in the initial ($t = 0$) values of velocities (not shown here) was found to be similar to the ones in Fig. 12. However the unsteady solutions, as expected, showed longer persistence (i.e. smaller “decay rates”) in the weakly attracting (i.e. smaller “attraction rates”) downstream portions of the flow. Recall that this paper has chosen the measure of “attraction rates” over “decay rates” because: (a) they are computationally easier to obtain, (b) they are physically meaningful even in the non-linear context (i. e. without the requirement of modeling time behavior by an exponential function of time), and (c) they also relate to physical attainability of steady flows. The response of the solution to disturbances when transverse downward component of gravity is present was also found to be equally stable because of the thinness of the film over the distances our computations could be implemented.

The above described response is different than the response [16] for the gravity driven external flow problem of Nusselt [7], where the gradually speeding condensate allows disturbances on the interface to grow only after a certain critical distance x and only for wavelengths $\lambda \geq \lambda_{\text{cr}}$, where λ_{cr} is a certain critical wavelength. For gravity-driven flows, it was this inertial instability associated with speeding condensate that marked the transition from smooth laminar to wavy laminar flows. This typically happened when the condensate Reynolds

number $\text{Re}_\delta (\equiv 4 \int_0^\Delta \rho_1 u_1(x, y) dy / \mu_1)$ - which represents the size of inertia to viscous forces

associated with fluctuations (a quantity which increases with x) - was computationally found to be higher than some critical value in the range of $20 \leq \text{Re}_\delta \leq 40$. In contrast, the above described

stable response for the Koh problem involved a much more weakly increasing Re_δ values with $Re_\delta \leq 10$.

Therefore the reasons for this external flow showing very strong and stable response to initial disturbances are:

- The condensate flow is slow because it is not driven by gravity, and hence, the mechanism for the wave evolution on the interface is very different as compared to the gravity driven flows in which the liquid condensate accelerates.
- The well defined far field pressure prescription of p_∞ (along AB and BD' in Fig. 1) and the process of condensation (mass transfer at the interface) make the flow more stable as compared to the known Kelvin Helmholtz instability (see [24] – [25]) for adiabatic (air water type) flows which do not involve gas-phase suction or mass transfer in to the liquid phase. As shown in Fig. 12, this well known dynamic instability for adiabatic flows is truly suppressed. This suppression of Kelvin Helmholtz instability for the interface is over and above the earlier described issue of delayed transition to turbulence in the vapor boundary layer due to vapor suction effects.

Despite the fact that, in the presence of non-zero interfacial mass flux, these flows show no instabilities over the distances considered, one still expects that at larger downstream distances, the flow will undergo transition to waviness whether or not transverse gravity is present.

6.3 Sensitivity of “Attractors”/Steady Solutions to Persistent Condensing-Surface Noise

Irrespective of their stability to initial disturbances superposed on the interface, the stable solutions obtained for this external condensing flow over a horizontal plate are found to be sensitive to small and persistent condensing-surface noise of standing wave types - whose single representative Fourier component is modeled as shown in Fig. 13. While response of condensing flows to these types of noise has been considered for internal condensing flows in [18]-[19] and also for an external condensing flow ([16]), this paper reports, for the first time, a quantitative analysis of the resulting wave forms along with a quantitative measurement of the resulting noise-sensitivity. The ever-present miniscule condensing surface noise is assumed to have a standing wave pattern in transverse displacement of the plate (of the type indicated in Fig. 13) with a representative Fourier component of the form:

$$\mathcal{D}_w(\chi, t) = \mathcal{D}_{\max} \sin \frac{2\pi\chi}{\lambda_p} \cdot \cos 2\pi f_p t \quad (18)$$

where, $\lambda_p (\equiv \lambda \cdot Y_e)$ is a physical wavelength (≥ 0.02 m), $f_p (\equiv f \cdot U_\infty / Y_e)$ is a physical frequency (0 - 15 Hz), and \mathcal{D}_{\max} is a physical amplitude (0 - 5 μm) with which the condensing-surface is likely to vibrate under typical ever-present noise conditions that are neither seen nor heard. The flow sees this noise through the following boundary condition for the vertical component of liquid velocity at the bottom wall location ($y = 0$):

$$v_1(\chi, 0, t) = v_{\max} \sin(2\pi\chi/\lambda_p) \cdot \sin(2\pi f_p t). \quad (19)$$

Since, $v_1(\chi, 0, t) = \partial \mathcal{D}_w(\chi, t) / \partial t$, it follows that the amplitude $v_{\max} (\equiv \varepsilon_w \cdot U_\infty)$ in Eq. (19) above is related to \mathcal{D}_{\max} in Eq. (18) by

$$v_{\max} = -2\pi\mathcal{D}_{\max}f_p . \quad (20)$$

It has been established – by post processing the details of the resulting wave forms – that the response of the interface is of the form

$$\Delta(x, t) - \Delta(x)_{\text{steady}} = \{a(x) \sin[(2\pi x/\lambda_p) + \gamma_0(t)] \cdot \cos[(2\pi f_p t) + \psi_0(x)]\}, \quad (21)$$

where, $a(x)$ is the x -dependent amplitude of the resulting standing wave pattern on the interface. Thus, waves on the interface, in response to the bottom wall noise, do have the same spatial wavelength λ_p and temporal frequency f_p as that of the displacement noise component $\mathcal{D}_w(x, t)$ experienced by the condensing-surface. However, the phases of the interfacial waves slightly differ from that of the condensing-surface's transverse displacement wave. The spatial phase difference is time dependent and is denoted by “ $\gamma_0(t)$ ” and the temporal phase difference is location dependent and is denoted by “ $\psi_0(x)$.” Figure 14 shows the unsteady interface at different times in response to the representative condensing-surface noise. For the cases considered in this paper, over a wide range of different affecting parameters, it is found that the amplitude $a(x)$ of these interfacial waves increases with x and can be determined. However spatial phase difference function $\gamma_0(t)$ is a sufficiently weak function of time and the temporal phase difference $\psi_0(x)$ is a sufficiently weak function of space that they cannot be determined, with sufficient precision, with the help of the simulation tool employed here. The spatially growing noise-induced waves are expected to be related to Re_δ values – which represents both the cross-sectional liquid mass-flux and the effects of local interfacial mass-flux \dot{m} . The noise-sensitive values of the amplitudes $a(x)$ ($\equiv a(x)/Y_e$) of these interfacial waves were computationally obtained for different flow cases for a range of different non-dimensional parameters viz. wavelength λ ($\equiv \lambda_p/Y_e$), bottom wall velocity amplitude ε_w ($\equiv v_{\max}/U_\infty$), and frequency f ($f \equiv 1/T_w \equiv f_p \cdot Y_e / U_\infty$). The

amplitude $a(x)$ values were measured by looking at several peak values of computationally obtained “ $\delta(x,t) - \delta(x)_{\text{steady}}$ ” signals in the space-time domain. After obtaining the values of $a(x)$ at different x locations, for different flow cases involving different D_{max} values, linear curves – as in Fig. 15 – were found to be adequate fits to the data of $a(x)$ over the range of distances considered. This linear relation can be expressed as

$$a(x)/D_{\text{max}} = \bar{c}_1 x + c_2 \quad (22)$$

where \bar{c}_1 and c_2 are respectively found to be 120.9 (m^{-1}) and 3.00 for R-113 flow parameters indicated in the inset of Fig. 15.

6.4 Non-attainability of Steady Film Flows at Lower Vapor Speeds

The computational results presented earlier in this paper were mainly for R113 vapor flows at speeds: $10 \text{ m/s} > U_\infty > 0.2 \text{ m/s}$. As one approaches the lower vapor speeds ($U_\infty \leq 0.2 \text{ m/s}$) in Fig. 16, unsteady solutions show non-existence of a steady long term ($t \rightarrow \infty$) limit that exists for $U_\infty > 0.2 \text{ m/s}$. One is tempted to say that the steady solutions for $U_\infty > 0.2 \text{ m/s}$ loses stability as speed U_∞ is lowered further but the situation is different because one does not find, at least computationally, a steady solution for $U_\infty < 0.2 \text{ m/s}$. Since one does not have a steady solution in this range, one cannot say that the steady solution for $U_\infty < 0.2 \text{ m/s}$ has lost its stability. This non-existence of a steady limit is a gradual phenomena which is depicted in Figure 16. The signs of non-existence of a steady limit is especially apparent in the aft portion of the flow for vapor speed $U_\infty = 0.08 \text{ m/s}$. This is different than noise-sensitive steady limits discussed earlier for higher speeds (also see $U_\infty = 0.2 \text{ m/s}$ in Fig. 16 which exhibits existence of a steady limit). This fact is more apparent through Fig. 17 which plots long term physical values of rate of change of film thickness ($\partial\Delta/\partial t$) at a fixed ‘ x ’ location ($x = 30$). It can be seen that as vapor

speed reduces below some critical value (below 0.2 m/s), the rate of change of film thickness starts increasing indicating above its effectively zero value (which is defined in Fig. 17, within computational errors, to be 1.5×10^{-7}). This sustained unsteadiness at such low vapor speeds implies non-attainment of any limiting steady solution of the film condensation type and one expects an eventual long time behavior that involves a more complex liquid-vapor morphology.

It is known that, as vapor speed reduces, the available shear stress for driving the thin liquid film reduces and, also, more kinetic energy of the vapor is deflected away from the condensate (the upward bending streamlines in Fig. 5 cover more of the leading edge and pressure gradients near the leading edge – as shown in Figs. 3-4 - become sharper). The gradualness of the loss of the above described steady limit (i. e. existence of steady film wise solution) is further demonstrated by insufficient availability of mechanical energy (i.e. near zero values of viscous dissipation rates in Fig. 18).

When we plot, in Fig. 18, the viscous dissipation rate ϕ (see Eq. (A13) in the Appendix) at which energy is dissipated in the interior of the vapor and the liquid phases inside any representative control volume for which long term steady solutions exist, it is observed that, as vapor speed decreases (and approaches values below $U_\infty = 0.2 - 0.3$ m/s), the dissipative energy *asymptotically* approaches negligible or near zero values. Figure 18 shows normalized dissipative energies (ϕ/ϕ_{ref}) as obtained by steady as well as long-term steady solutions of this problem in a representative control volume defined by $0 < x < 40$ and $0 < y < 0.5$. Even though the energy dissipated in any control volume depends on its size, it was observed that the normalized values follow exactly the same trend irrespective of the size of the control volume. Here the normalizing dissipation rate ϕ_{ref} is the value of ϕ for the chosen control volume at speed $U_\infty = 3$ m/s. In Fig. 18, the value of $\phi_{\text{ref}} = 3.48 \times 10^{-2}$ W for $U_\infty = 3$ m/s and a control

volume defined by $0 < x < 40$ and $0 < y < 0.5$. For vapor speeds between $1 \text{ m/s} < U_\infty < 3 \text{ m/s}$, the thick line in Fig. 18 shows ϕ/ϕ_{ref} values as obtained from the steady solutions while the dotted line in Fig. 18 shows ϕ/ϕ_{ref} values obtained from long-term steady limits of unsteady solutions for $0.2 \text{ m/s} < U_\infty < 3 \text{ m/s}$. There were some algorithmic issues in the steady solver for $0.2 \text{ m/s} < U_\infty < 1 \text{ m/s}$ whose improvements were not considered necessary and therefore were not included for results in Fig. 18. It should be noted that the integral *theorem on expended mechanical power* (see Ch. 15, [26]) or the integral form of *mechanical energy equation* (see Eq. (5.4.13) of [27]) says that a steady solution exists if and only if $\phi/\phi_{\text{ref}} > 0$ and this condition is hard to satisfy in Fig. 18 for $0 \text{ m/s} < U_\infty < 0.2 \text{ m/s}$ because the energy for $U_\infty = 0$, where the theorem is violated, is effectively equivalent to the energy at $U_\infty = 0.2 \text{ m/s}$. This fact that energy available to dissipate at $U_\infty < 0.2 \text{ m/s}$ (say $U_\infty = 0.08 \text{ m/s}$) is effectively the zero value associated with $U_\infty = 0$ should lead to a response that is also somewhat similar to what is expected at $U_\infty = 0$ and fixed $\Delta\mathcal{T}$. Clearly, for $U_\infty = 0$ and fixed $\Delta\mathcal{T}$, one expects a rising unsteady film type solution which is similar to what is being found in Fig. 17. However the flow for $0 < U_\infty < 0.2 \text{ m/s}$ also has an option to come to a new quasi-steady flow under a more complex liquid/vapor morphology.

Because of the mutually supportive nature of the above described independent facts, one can reliably state that film wise steady condensation solution for this problem is not possible for effectively zero inlet speeds that correspond to a certain finite range of values of the type: $0 < U_\infty < U_\infty^*$. This result states that Koh solution [2] for $0 < U_\infty < U_\infty^*$ is not valid.

6.5 Additional Sensitivity of These Shear Driven Flows

The above described steady solution, under uniform far field pressure ($p = p_\infty$) assumption, shows stability for $U_\infty > U_\infty^*$ with possible attainability issues (for non-zero transverse gravity) and increasing waviness issues only after a sufficiently large downstream distance x . Note that shear driven film condensation flows are extremely sensitive because, unlike gravity driven flows, the liquid condensate motion is driven by vapor motion and it takes minuscule pressure differences to change vapor motion. Therefore any difficulty in experimentally achieving far field uniform pressure ($p = p_\infty$) condition – particularly near the downstream zones of far field locations – will additionally limit the attainability of steady film wise condensation for this problem. Furthermore, besides the fact that similar sensitivity is found for shear driven internal condensing flows (as described in the Introduction), the role of various boundary conditions were also discussed, for finite horizontal plates, by Prasad and Jaluria [28]. It should be further noted that these “structural” sensitivities and instabilities associated with shear driven annular or film condensation flows are not present for the gravity driven condensing flows ([7], [16]).

7. Conclusions

- For the ranges of the flow parameters investigated, the Koh solution [2] for film thickness is found to be reasonably accurate for horizontal condensing flows over a flat plate under conditions of sufficiently fast vapor speeds and nearly uniform far field pressure p_∞ . Over this range, it is found that, there is some departure from the Koh solution [2] in the frontal portion of the plate with regard to the values of interfacial velocities and pressure variations in the

liquid and vapor domains. The gradients in pressure become sharper as vapor speed reduces and such dynamics cannot be captured using analytical solution of Koh [2].

- The results show that the presence or absence of transverse component of gravity does not change the steady solution by much if only a certain length from the leading edge (lengths investigated here) is considered. Over this length only changes in the hydrostatic pressure variations, resulting from presence or absence of gravitational component of pressure, are observed in the liquid film.
- For the ranges of the flow parameters investigated here for R113, unsteady solutions predicted that there exists a long-term ($t \rightarrow \infty$) steady solution (*attractor*) for this external condensing flow problem. A measure termed “attraction rate” is introduced for the reported “non-linear” stability analysis. This value decreases with increasing distance and increases with increasing vapor speeds. The qualitative and quantitative variation in the strength of the attractor is presented for the cases of $U_\infty > 0.2$ m/s. Unsteady results, along with several supporting results, find that at low vapor speeds ($0 < U_\infty < U_\infty^* \approx 0.2$ m/s) a film wise steady solution does not exist.
- It is established here that the steady solutions for sufficiently fast external flows and up to certain downstream distances are sensitive to persistent noise leading to increasing wave amplitudes with distance. However the smooth underlying steady solutions for these cases are stable to the momentary initial disturbances (of various wavelengths and amplitudes) on the interface.
- The computational results and physics indicate that the stable attracting solutions for this condensing flow over a horizontal plate are not only expected to become very sensitive, at large downstream distances, to persistent but minuscule condensing-surface noise but, also,

perhaps to presence of transverse gravity and any experimental difficulties in maintaining uniform pressure conditions in the far field downstream regions.

Acknowledgment

This work was supported by NASA grant NNC04GB52G.

Appendix

The differential forms of mass, momentum (x and y components) and energy equations in terms of non-dimensional variables for flows in the interior of either of the phases ($I = 1$ or 2) for this external flow are given as

$$\frac{\partial u_I}{\partial x} + \frac{\partial v_I}{\partial y} = 0 \quad (\text{A.1})$$

$$\frac{\partial u_I}{\partial t} + u_I \frac{\partial u_I}{\partial x} + v_I \frac{\partial u_I}{\partial y} = - \left(\frac{\partial \pi_I}{\partial x} \right) + \frac{1}{\text{Re}_I} \left(\frac{\partial^2 u_I}{\partial x^2} + \frac{\partial^2 u_I}{\partial y^2} \right) \quad (\text{A.2})$$

$$\frac{\partial v_I}{\partial t} + u_I \frac{\partial v_I}{\partial x} + v_I \frac{\partial v_I}{\partial y} = - \left(\frac{\partial \pi_I}{\partial y} \right) + \text{Fr}_y^{-1} + \frac{1}{\text{Re}_I} \left(\frac{\partial^2 v_I}{\partial x^2} + \frac{\partial^2 v_I}{\partial y^2} \right) \quad (\text{A.3})$$

$$\frac{\partial \theta_I}{\partial t} + u_I \frac{\partial \theta_I}{\partial x} + v_I \frac{\partial \theta_I}{\partial y} \approx \frac{1}{\text{Re}_I \text{Pr}_I} \left(\frac{\partial^2 \theta_I}{\partial x^2} + \frac{\partial^2 \theta_I}{\partial y^2} \right), \quad (\text{A.4})$$

where $\text{Re}_I \equiv \rho_I U_\infty Y_c / \mu_I$, $\text{Pr}_I \equiv \mu_I C_{pI} / k_I$, and $\text{Fr}_y^{-1} \equiv g_y Y_c / U_\infty^2$.

The term $[t]$ on the right side of Eq. (4) is given by:

$$[t] = \left\{ \frac{\mu_2}{\mu_1} \frac{\partial v_2}{\partial x} \right\}^i - \left\{ \frac{\partial v_1}{\partial x} \right\}^i + \frac{2\delta_x}{[1-\delta_x^2]} \left\{ \frac{\partial u_1}{\partial x} \right\}^i - \left\{ \frac{\partial v_1}{\partial y} \right\}^i - \frac{2\delta_x}{[1-\delta_x^2]} \frac{\mu_2}{\mu_1} \left\{ \frac{\partial u_2}{\partial x} \right\}^i - \left\{ \frac{\partial v_2}{\partial y} \right\}^i + \frac{\text{Ma} \left(\partial \pi_2 / \partial x \right)^i}{\sqrt{1+\delta_x^2}} \quad (\text{A.5})$$

where, $\text{Ma} \equiv \rho_2 U_\infty c_1 d_1 / \mu_1$ is a Marangoni number, $c_1 \equiv dT_s/dp$, and $d_1 \equiv -d\sigma/dT$.

Under assumptions of: uniform pressure throughout the flow, steadiness ($\partial/\partial t = 0$), horizontalness ($g_x = 0$), and boundary layer approximations ($\partial/\partial x \ll \partial/\partial y$ & $v_1 \ll u_1$) associated with thin condensate flow; the Koh formulation ([2]) effectively replaces (A.2) - (A.4) above by:

$$\begin{aligned}
u_1 \frac{\partial u_1}{\partial x} + v_1 \frac{\partial u_1}{\partial y} &\cong \frac{1}{Re_1} \frac{\partial^2 u_1}{\partial y^2}, \\
-\frac{\partial \pi_1}{\partial y} + Fr_y^{-1} &\cong 0, \text{ and} \\
u_1 \frac{\partial \theta_1}{\partial x} + v_1 \frac{\partial \theta_1}{\partial y} &\approx \frac{1}{Re_1 Pr_1} \left(\frac{\partial^2 \theta_1}{\partial y^2} \right). \tag{A.6}
\end{aligned}$$

In addition to the above, the Koh formulation [2] also assumes negligible interfacial slope approximation $(\delta'(x))^2 \ll 1$ and, as a result, interface conditions given by Eqs. (2)-(6) in the section 2 are simplified and respectively replaced by eqs. (A.7) - (A.11) given below:

$$u_2^i = u_1^i \tag{A.7}$$

$$\pi_1^i = \frac{\rho_2}{\rho_1} \pi_2^i, \tag{A.8}$$

$$\left. \frac{\partial u_1}{\partial y} \right|^i = \frac{\mu_2}{\mu_1} \left. \frac{\partial u_2}{\partial y} \right|^i, \tag{A.9}$$

$$\begin{aligned}
\dot{m}_{LK} &\equiv \left[u_1^i (d\delta/dx) - v_1^i \right], \\
\dot{m}_{VK} &\equiv (\rho_2/\rho_1) \left[u_2^i (d\delta/dx) - v_2^i \right], \text{ and} \tag{A.10}
\end{aligned}$$

$$\dot{m}_{Energy} \equiv Ja/(Re_1 Pr_1) \{ \partial \theta_1 / \partial y \big|^i - (k_2/k_1) \partial \theta_2 / \partial y \big|^i \}. \tag{A.11}$$

The remaining interface conditions given by Eqs. (7)-(8) in section 2 continue to hold as they need no further approximations. Furthermore, for the Koh formulation [2], no top or exit condition regarding pressure is necessary. Instead, the inlet and the far-field conditions respectively become:

$$u_2(0,y) = U_\infty, \text{ and } \lim_{y \rightarrow \infty} u_2(x,y) = U_\infty. \tag{A.12}$$

Total *integral* viscous dissipation rate ϕ ($= \phi_1 + \phi_2$) inside any control volume is obtained from *power law theorem* ([26]) or the integral form of *mechanical energy equation* (see [27]) for individual liquid and vapor domains and then adding them together. For any control-

volume “CVf –total” of the type OABD in Fig. 1, if one denotes the liquid-vapor interface by Σ , the bounding surface by “CSf-total,” unit normal on the bounding surface by \mathbf{n} , it results in the following expression:

$$\Phi = \int_{\text{CSf-total}} -p_{\text{rel}}(\mathbf{n} \cdot \mathbf{V})d\mathbf{a} + \int_{\Sigma} \left[\frac{\dot{m}}{\rho_1} - \frac{\dot{m}}{\rho_2} \right] p_{\text{rel}} d\mathbf{a} - 0.5 \int_{\text{CSf-total}} \rho |\mathbf{V}|^2 (\mathbf{n} \cdot \mathbf{V}) d\mathbf{a} - 0.5 \int_{\text{CSf-total}} \dot{m} \left[|\mathbf{V}_2|^2 - |\mathbf{V}_1|^2 \right] d\mathbf{a} \quad , \quad (\text{A.13})$$

where $p_{\text{rel}} \equiv p - p_{\infty}$ is the relative value of absolute pressure $p = p_I$ ($I = 1$ Or 2) with respect to the far field pressure p_{∞} .

References

1. Cess, R. D., 1960, “Laminar Film Condensation on a Flat Plate in the Absence of a Body Force,” *Zeitschrift für Angewandte Mathematik und Physik*, 11, pp. 426-433.
2. Koh, J. C. Y., 1962, “Film Condensation in a Forced-Convection Boundary-Layer Flow,” *International Journal of Heat and Mass Transfer*, Vol. 5, pp. 941-954.
3. Rose, J. W., 1998, “Condensation Heat Transfer Fundamentals,” Feb 1998, Trans. I Chem E, Vol. 76, Part A.
4. Balasubramaniam R., V. Nayagam, M. M. Hasan, and L. Khan, 2006, “Analysis of Heat and Mass Transfer During Condensation over a Porous Substrate,” *Annals of the Newyork Academy of Sciences*, 1077: 459-470.
5. Sparrow, E. M. and G. L. Gregg, 1959, “A Boundary Layer Treatment of Laminar Film Condensation,” *ASME J. Heat Transfer*, 81, pp. 13-18.
6. Koh, J. C. Y., E. M. Sparrow, and J. P. Hartnett, 1961, “The Two-phase Boundary Layer in Laminar Film Condensation,” *Int. J. Heat and Mass Transfer*, 2, pp. 69-82.
7. Nusselt, W., 1916, “Die Oberflächenkondensation des Wasserdampfes,” *Z. Ver. Dt. Ing.* 60 (27), pp. 541-546.
8. Incropera, F. P. and D. P. DeWitt, 1996, *Fundamentals of Heat and Mass Transfer*, Fourth

Edition, Wiley.

9. S. Mitra, A. Narain, S. Kulkarni, R. Naik, and J. H. Kurita, "Annular /Stratified Internal Condensing Flows in Millimeter to Micrometer Scale Ducts," MNHMT 2009-18507, Proceedings of ASME 2nd Micro/Nanoscale Heat & Mass Transfer International Conference, December 18-22, 2009, Shanghai, China.
10. Rabas, T. J., and B. Arman, 2000, "Effects of the Exit Condition on the Performance of In-Tube Condensers," *Heat Transfer Engineering*, 21(1), pp. 4-14.
11. Chen, Y. P., and P. Cheng, 2005, "Condensation of Steam in Silicon Microchannels," *Int. Comm. of Heat Mass Transfer*, v.32, pp.175-183.
12. Wu, H. Y., and P. Cheng, 2005, "Condensation Flow Patterns in Microchannels," *Int. J Heat Mass Transfer*, v.48, pp.2186-297.
13. Coleman, J. W., S. Garimella, 2003, "Two-phase Flow Regimes in Round, Square, and Rectangular Tubes during Condensation of Refrigerant R134a, *Int. J. Refrig.*, 26, pp. 117-128.
14. Garimella, S., 2004, "Condensation Flow Mechanisms in Microchannels: basis for Pressure Drop and Heat Transfer Models," *Heat Transfer Eng.*, 25, pp. 104-166.
15. Mitra, S., A. Narain, S. D. Kulkarni, J. Kurita, M. Kivisalu, and M. M. Hasan, 2009, "Shear Driven and Gravity Driven Annular/Stratified Internal Condensing Flows," Submitted for publication in the *International Journal of Transport Processes*.
16. Phan, L. and A. Narain, 2007, "Non-linear Stability of the Classical Nusselt problem of Film Condensation and Wave Effects," *ASME Journal of Applied Mechanics*, Vol.74, No.2, pp. 279-290.
17. Narain A., J. H. Kurita, M. Kivisalu, A. Siemionko, S. Kulkarni, T. Ng., N. Kim, and L.

- Phan, 2007, "Internal Condensing Flows inside a Vertical Pipe – Experimental/Computational Investigations of the Effects of Specified and Unspecified (Free) Exit Conditions at Exit," *Journal of Heat Transfer*, Vol. 129, Oct 2007.
18. Narain, A., Q. Liang, G. Yu, and X. Wang, 2004, "Direct Computational Simulations for Internal Condensing Flows and Results on Attainability/Stability of Steady Solutions, Their Intrinsic Waviness and Their Noise-Sensitivity," *Journal of Applied Mechanics*, Vol. 71, pp. 69-88.
 19. Liang, Q., X. Wang, and A. Narain, 2004, "Effect of Gravity, Shear and Surface Tension in Internal Condensing Flows - Results from Direct Computational Simulations," *ASME Journal of Heat Transfer*, 126 (5), pp. 676-686.
 20. Phan L., X. Wang, and A. Narain, 2006, "Exit Condition, Gravity and Surface-Tension Effects on Stability and Noise Sensitivity Issues for Steady Condensing Flows inside Tubes and Channels," *International Journal of Heat and Mass Transfer*, Vol. 49, Issues 13-14, pp. 2058-2076.
 21. Carey, V. P., 1992, *Liquid-Vapor Phase-Change Phenomena*, Series in Chemical and Mechanical Engineering, Hemisphere Publishing Corporation.
 22. Delhaye, J. M., 1974, "Jump Conditions and Entropy Sources in Two-phase Systems; Local Instant Formulation," *Int. J. of Multiphase Flow*, 1, pp. 395-409.
 23. Schlichting, H., 1968, *Boundary Layer Theory*, Sixth Edition, McGraw Hill.
 24. Turner, J. S., 1973, *Buoyancy Effects in Fluids*, Cambridge University Press, London.
 25. Kundu, P. K., 1990, *Fluid Mechanics*, Academic Press, Sandiego, CA, USA.
 26. Gurtin, M. E., 1981, *An Introduction to Continuum Mechanics*, Academic Press, New York.
 27. Whitaker, S., 1977, *Fundamental Principles of Heat Transfer*, Pergamon Press, New York.

28. Prasad, V. and Jaluria, Y., 1982, "Chemical Engineering Communications," Vol. 13, pp. 327-342.

Figure Captions:

Fig. 1: The figure shows a schematic for a typical finite computational domain for a film condensation flow over a horizontal plate due to a forced uniform vapor flow at the left inlet.

Fig. 2: For flow of R113 vapor with $U_\infty = 2$ m/s, $\Delta T = 5^\circ\text{C}$, $p_\infty = 1$ atm, $x_e = 45$, $g_y = 0$, and $Y_e = 0.004$ m, this figure compares non-dimensional film thickness (δ) values for the steady solution (obtained from solving the steady governing equations) with those obtained from Koh's similarity solution [2].

Fig. 3: For the steady solution of Fig. 2, this figure shows, at a fixed $y = 0.8$ location, computationally obtained variation of non-dimensional pressure π_2 with non-dimensional distance x .

Fig. 4: For the steady solution of Fig. 2, Fig. 4 shows computationally obtained y-directional variation of non-dimensional pressure π across different cross sections along the domain. The pressure in vapor domain above condensate film is represented by π_2 and pressure in liquid domain below the interface is represented by $(\rho_1/\rho_2) \pi_1$.

Fig. 5: The figure shows the streamline pattern for the case in Fig. 2. The pattern is obtained from the reported simulation technique. The contour on the background represents the magnitude of u_I velocities.

Fig. 6: For the steady solution of Fig. 2, this figure compares non-dimensional values of x-directional liquid velocities at the interface (u_1^i) as obtained from the similarity solution [2] with those obtained from the computational solution.

Fig. 7: For flow of R113 vapor with $U_\infty = 2$ m/s, $\Delta T = 5^\circ\text{C}$, $p_\infty = 1$ atm, $x_e = 50$, and $g_y = 0$, this figure compares non-dimensional values of film thickness δ obtained from simulations for the same steady conditions under two different choices of grids ($n_i \times n_j$) and domain heights Y_e . Grid 1 corresponds to the grid size of 30×50 with $Y_{e1} = 0.004$ m and Grid 2 corresponds to the grid size of 35×70 with $Y_{e2} = 0.008$ m. Non-dimensional values of δ and x for grid 2 are converted and compared in terms of grid 1 (by multiplying them by Y_{e2}/Y_{e1}).

Fig. 8: For flow of R113 vapor with $U_\infty = 1.7$ m/s, $\Delta T = 5^\circ\text{C}$, and $g_y = 0$, this figure shows non-dimensional film thickness values at different non-dimensional times given by the unsteady solution of the problem. An initial guess given at time $t = 0$ (about 16 % below the final long term solution) is seen to get attracted to the long term steady solution at different rates. The markings, at different times, demarcate the zones that have “nearly” converged to the steady solution from the zones that have not.

Fig. 9: For flow of R113 with $U_\infty = 1.7$ m/s, $\Delta T = 5^\circ\text{C}$ and $g_y = 0$, this figure shows different rates of attraction versus time - as indicated by different representative deceleration rates - for different χ values along the length of the plate. The value of the initial attraction rate $\partial\Delta/\partial t(\chi, 0) \equiv \partial\Delta/\partial t|_{\text{init}}$ as well as the “strength” of the attractors (as marked by the representative magnitude of deceleration rates associated with the slopes of the lines AB, A'B', etc.) decrease with increasing χ . The initial guess of $\delta(x, 0)$ for the unsteady solution was 16% below the long term steady solution.

Fig. 10: For flow of R113 with $\Delta T = 5^\circ\text{C}$, $g_y = 0$, and $x = 30$, the figure shows different rates of attraction versus time - as indicated by different representative magnitudes of deceleration rates associated with the slopes of the lines AB, A'B', etc. - at different vapor speeds. The initial guess of $\delta(x,0)$ for the unsteady solution was 16% below the long term steady solution. The figure demonstrates higher rates of attraction for higher speeds.

Fig. 11: This figure shows computationally obtained curves depicting the rate of change of film thickness at $x = 23$ when the unsteady solutions approach the same long-term steady attractor from three different initial guesses for flow of R-113 vapor at $U_\infty = 2 \text{ m/s}$, $g_y = 0$ and $\Delta T = 5^\circ \text{C}$. The three initial guesses 1, 2, and 3 are respectively 2 %, 5 %, and 7 % away from the unique long-term steady attractor. The subsequent time duration (marked τ_{Rep}) over which a nearly constant deceleration rate ($\partial^2 \Delta / \partial t^2$) exists is marked by nearly equal constant decelerating slopes of lines AB, A'B', A"B" on curves X, Y, and Z. This shows that for a given vapor speed, the above characterized attraction rates over τ_{Rep} are associated with the long term steady solutions rather than the values of the initial guesses.

Fig. 12: For flow of R113 vapor with $U_\infty = 3 \text{ m/s}$, $x_e = 50$, $\Delta T = 5^\circ\text{C}$, $g_y = 0$, this figure shows the stable response of the long term steady solution to the rather large initial disturbance given at time $t = 0$. The non-dimensional disturbance is given as $\delta(x, 0) = \delta_{\text{steady}}(x) [1 + \varepsilon_0 \delta'(x, 0)]$, where $\delta'(x, 0) \equiv \sin(2\pi x / \lambda_0)$, $\varepsilon_0 = 0.35$ and $\lambda_0 = 5$. The disturbance dies out, almost completely, by the time $t = 1500$.

Fig. 13: This figure depicts the definition of the type of miniscule ever-present noise given to the condensing surface to investigate the sensitivity of condensing flows to persistent disturbances.

The inset shows the displacement profile of the condensing surface at two out-of-phase instants associated with a mode of the standing wave.

Fig. 14: For R113 vapor with $U_\infty = 3$ m/s, $x_e = 48$, $\Delta T = 5^\circ\text{C}$, $g_y = 0$, this figure shows unsteady response of the flow to the typical condensing surface noise with $\lambda (\equiv \lambda_p/Y_e) = 10$, $T_w (\equiv U_\infty/(f_p \cdot Y_e)) = 240$, $\varepsilon_w (\equiv v_{\max}/U_\infty) = 3 \cdot 10^{-6}$. The noise given to the condensing surface is represented as $v_1(x, 0, t) = v_{\max} \sin(2\pi x/\lambda_p) \cdot \sin(2\pi f_p t)$, where $v_1(x, 0, t)$ is condensing surface velocity. Figure shows non-dimensional film thickness $\delta(x, t)$ plotted vs. x at two different non-dimensional times $t = 140$ and $t = 260$. The steady film thickness values $\delta(x)_{\text{steady}}$ are shown as an initial solution at time $t = 0$.

Fig. 15: For different ranges of condensing surface noise parameters, namely: time period T , wavelength λ , and condensing surface velocity vibration amplitude ε_w , and different vapor speeds U_∞ ; this figure plots computationally obtained non-dimensional a/D_{\max} values (amplitude of interfacial waves divided by amplitude of bottom wall displacement waves) against dimensional values of $x (= x \cdot Y_e)$. The range of R-113 vapor (with $g_y = 0$) flows considered here is described in the inset.

Fig. 16: The figure plots two different sets (for $U_\infty = 0.2$ m/s and $U_\infty = 0.08$ m/s,) of long term film thickness values $\delta(x, t)$ with x at large non-dimensional times $t = 22$ s and 34 s. The flows are of R113 vapor at $\Delta T = 5^\circ\text{C}$ and initial conditions (not shown) for each of these cases was the Koh similarity solution [2]. For $U_\infty < 0.2$ m/s, the aft portions of these curves suggest non-existence of $\lim_{t \rightarrow \infty} \delta(x, t)$

Fig. 17: The figure plots long term steadiness measure $\left| \frac{\partial \Delta}{\partial t} \right|$ (estimated at $x = 40$) with free stream speed U_∞ . The flows are of R113 vapor at $\Delta T = 5^\circ\text{C}$. The values of $\left| \frac{\partial \Delta}{\partial t} \right|$ for $U_\infty > 0.2$ m/s is considered effectively zero within computational error. This suggests existence of a long time steady solution. However the rising positive values of $\left| \frac{\partial \Delta}{\partial t} \right|$ for $U_\infty < 0.2$ m/s suggest non-existence of a long time steady solution.

Fig. 18: For flow of R113 vapor with $\Delta T = 5^\circ\text{C}$, $X_e = 0.2$ m, and $g_y = 0$, this figure plots normalized viscous dissipation rates ϕ/ϕ_{ref} (see Eq. (A.13) in the Appendix for the definition of ϕ) obtained from steady and unsteady (long-term) steady solutions in a representative control volume given by $0 < x < 40$ and $0 < y < 0.5$. As the vapor speed U_∞ reduces below 0.2 m/s, dissipation rates can be seen becoming effectively equal to the zero value associated with $U_\infty = 0$.

Figures:

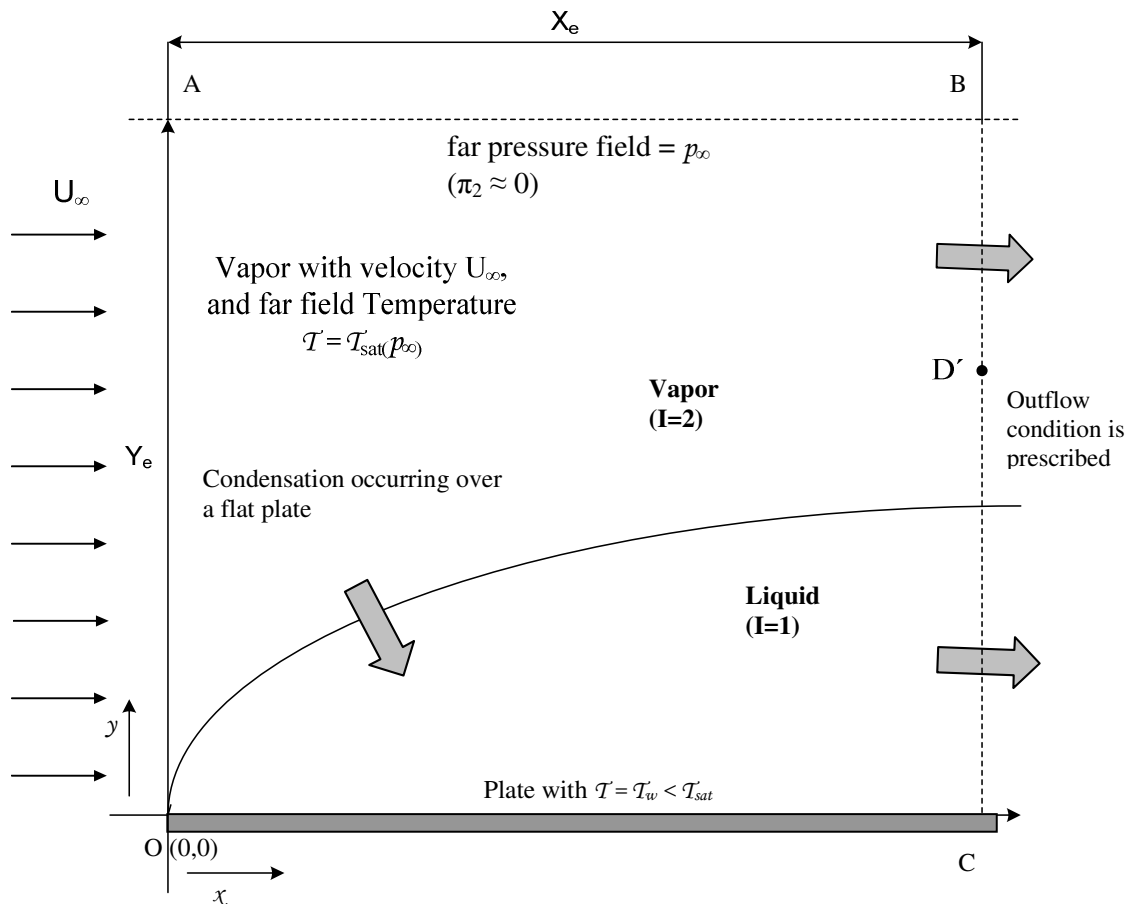


Fig. 1

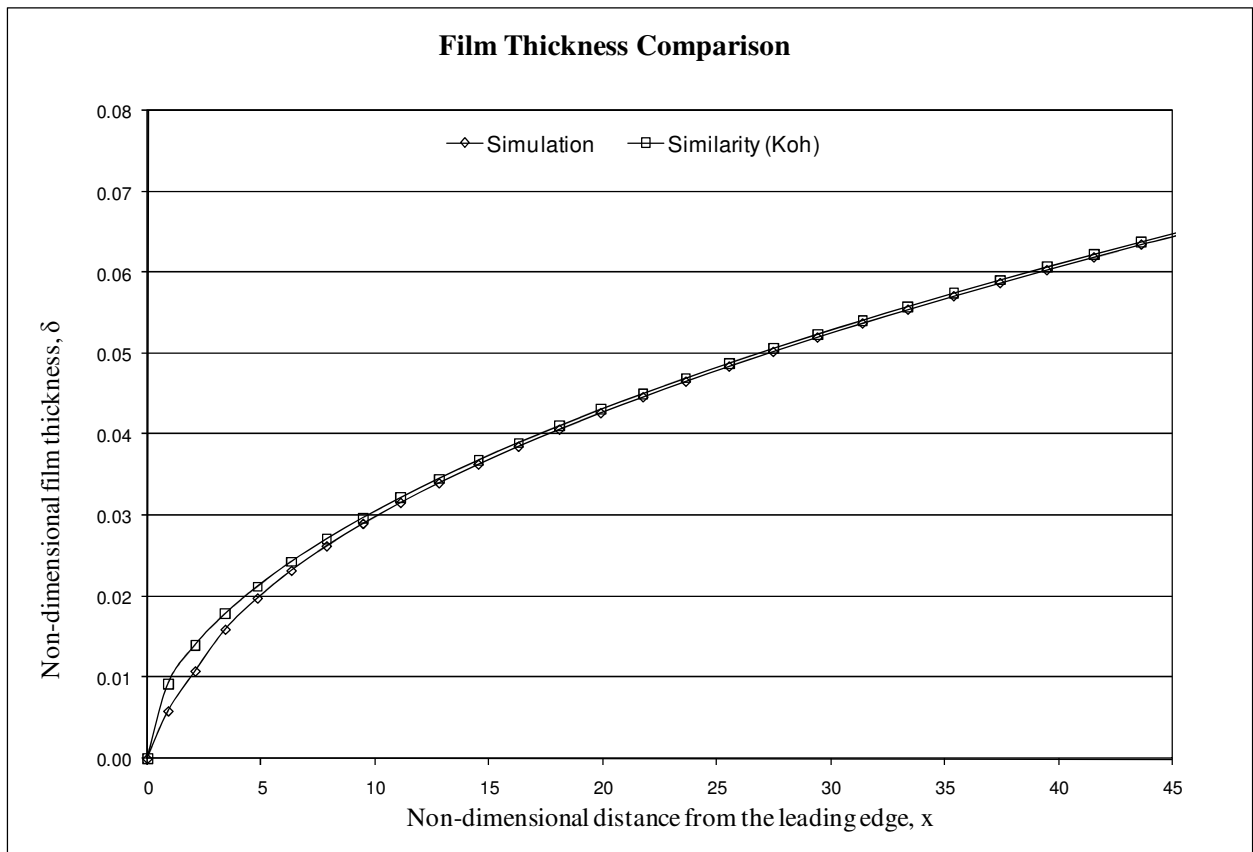


Fig. 2

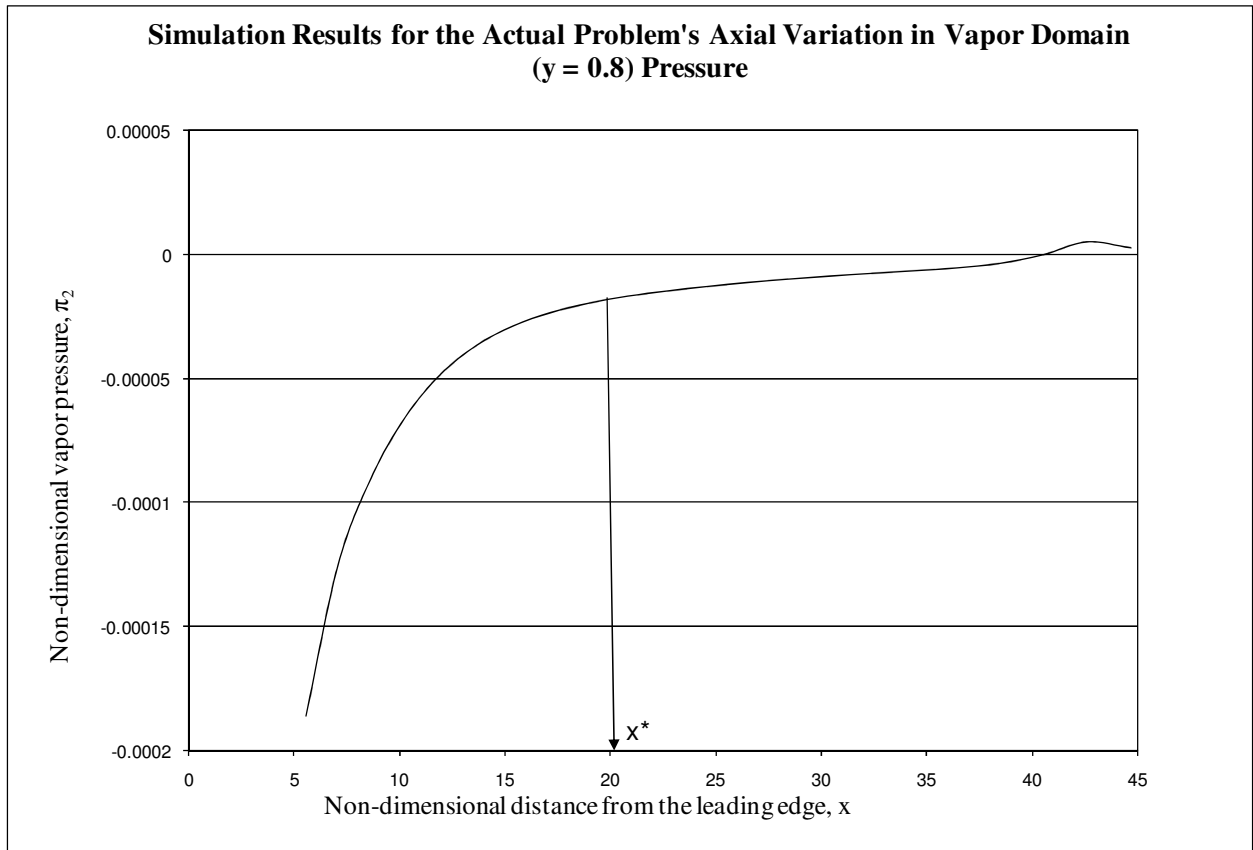


Fig. 3

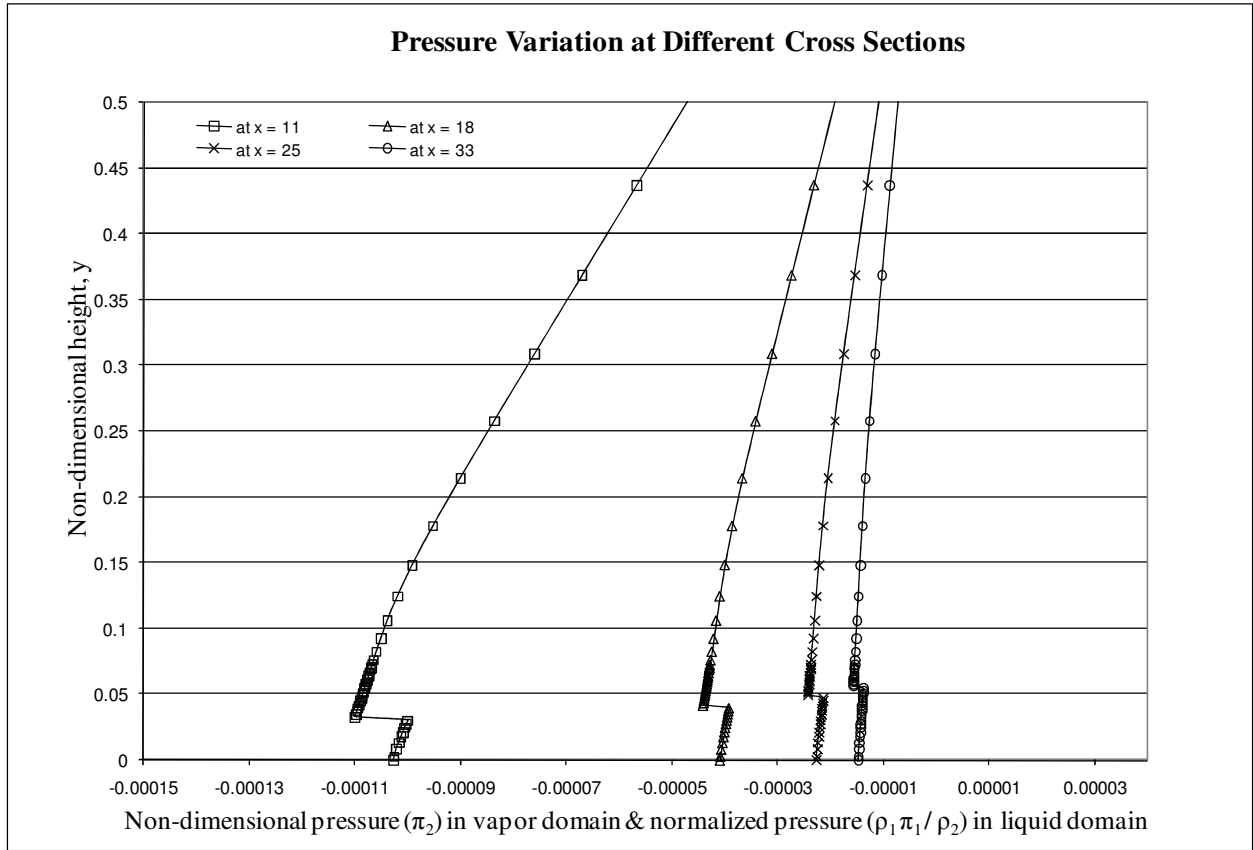


Fig. 4

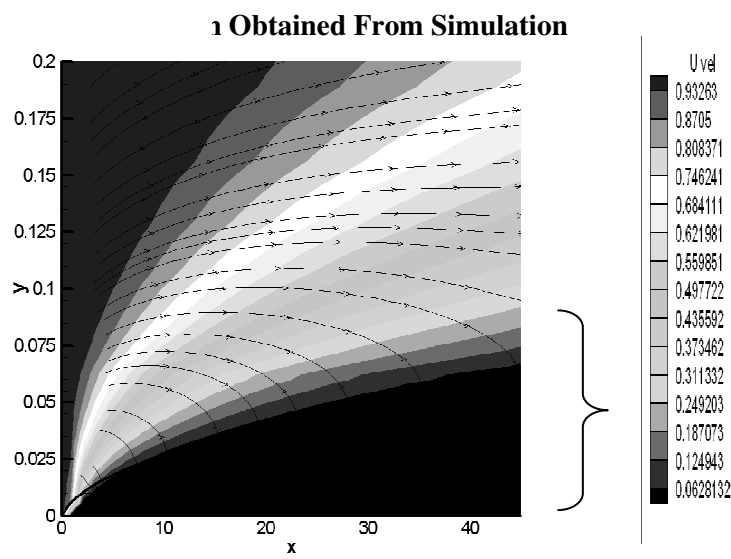


Fig. 5

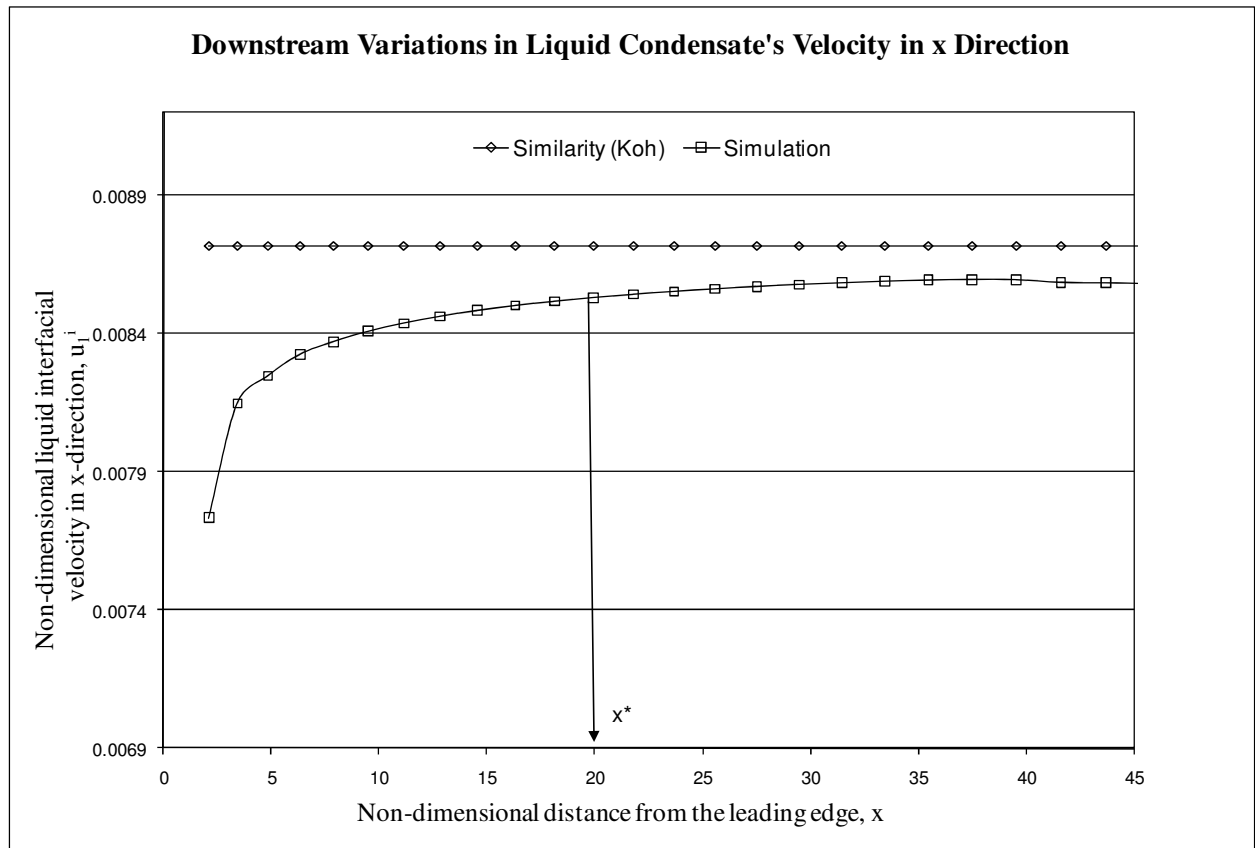


Fig. 6

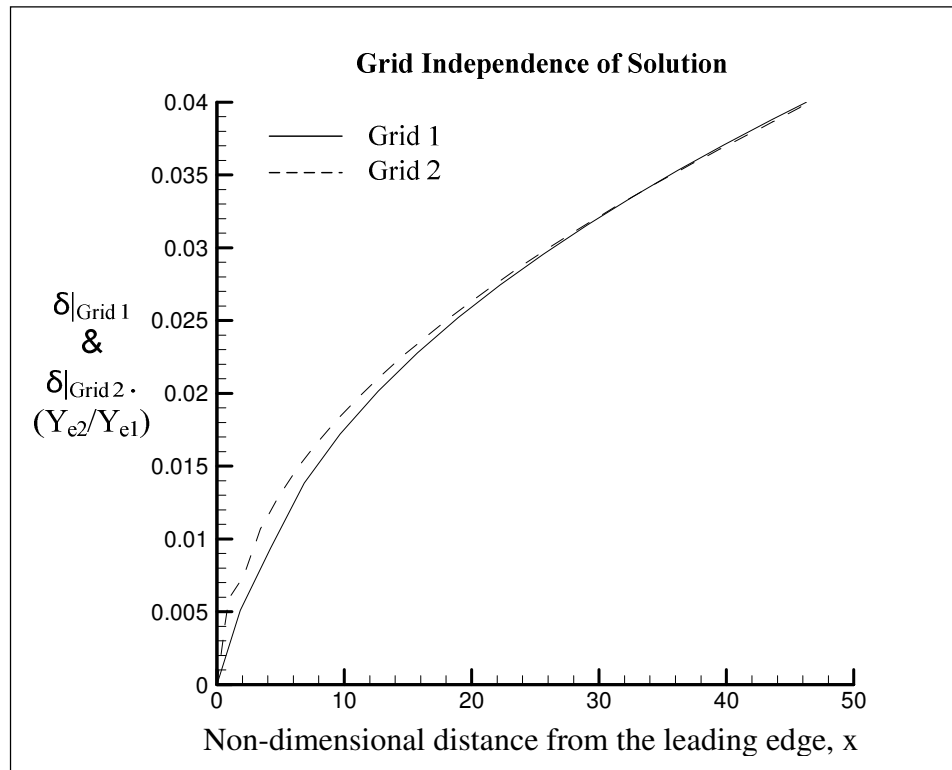


Fig. 7

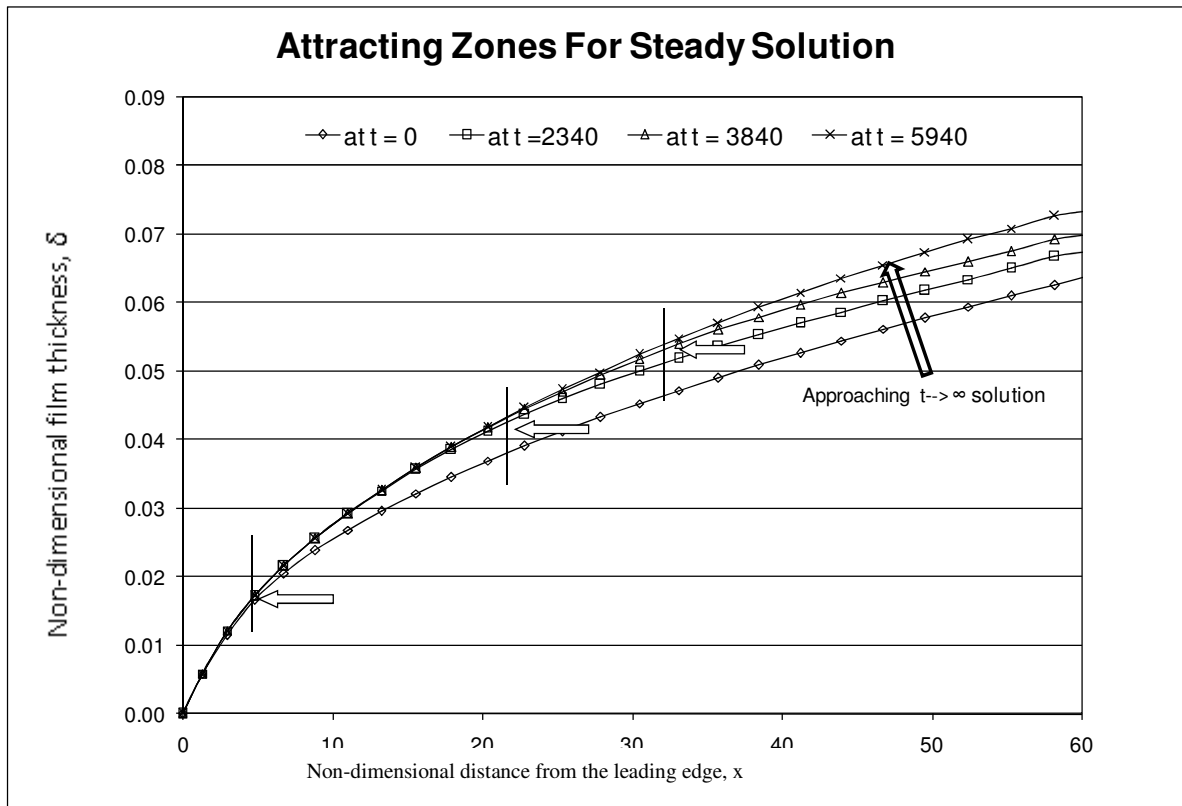


Fig. 8

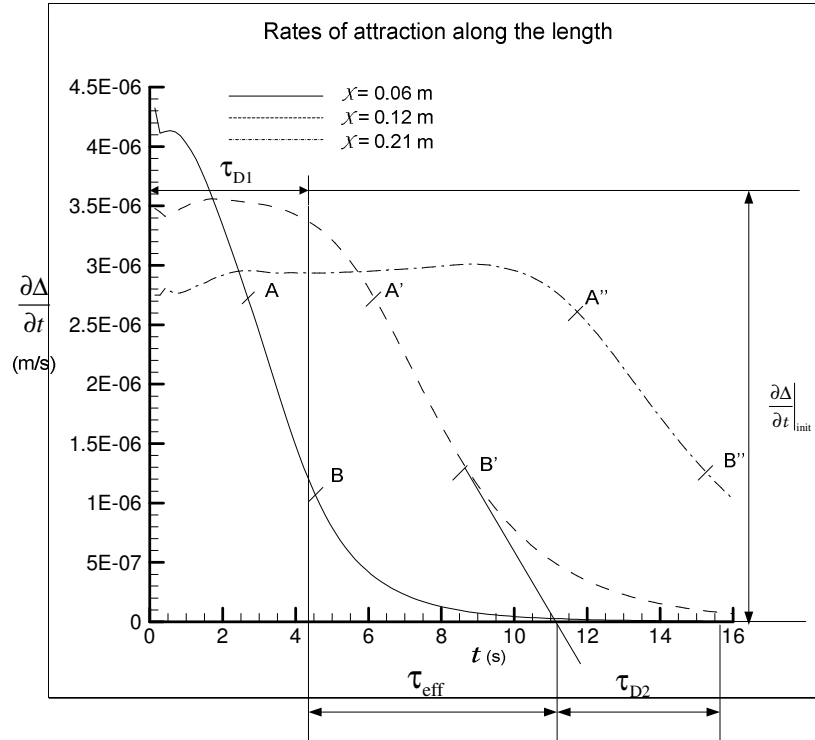


Fig. 9

Rates of attraction at different speeds

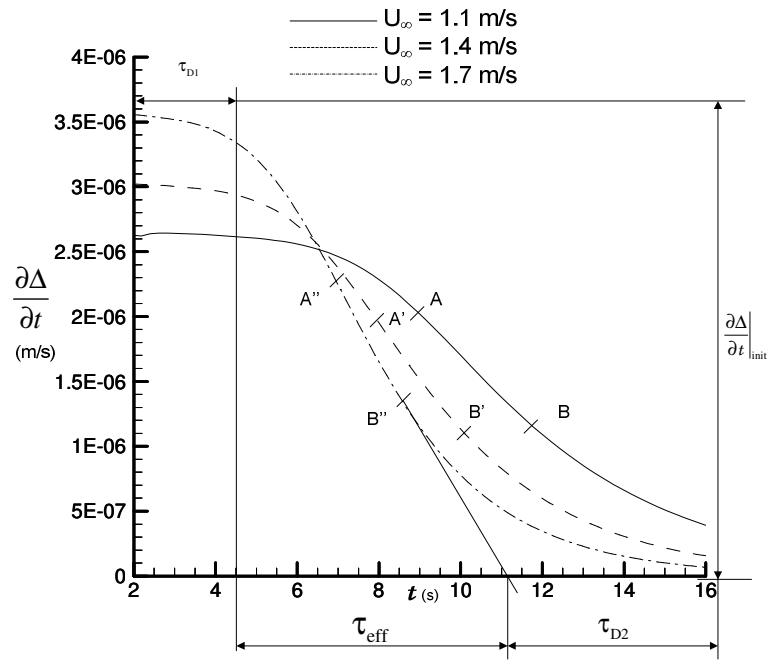


Fig. 10

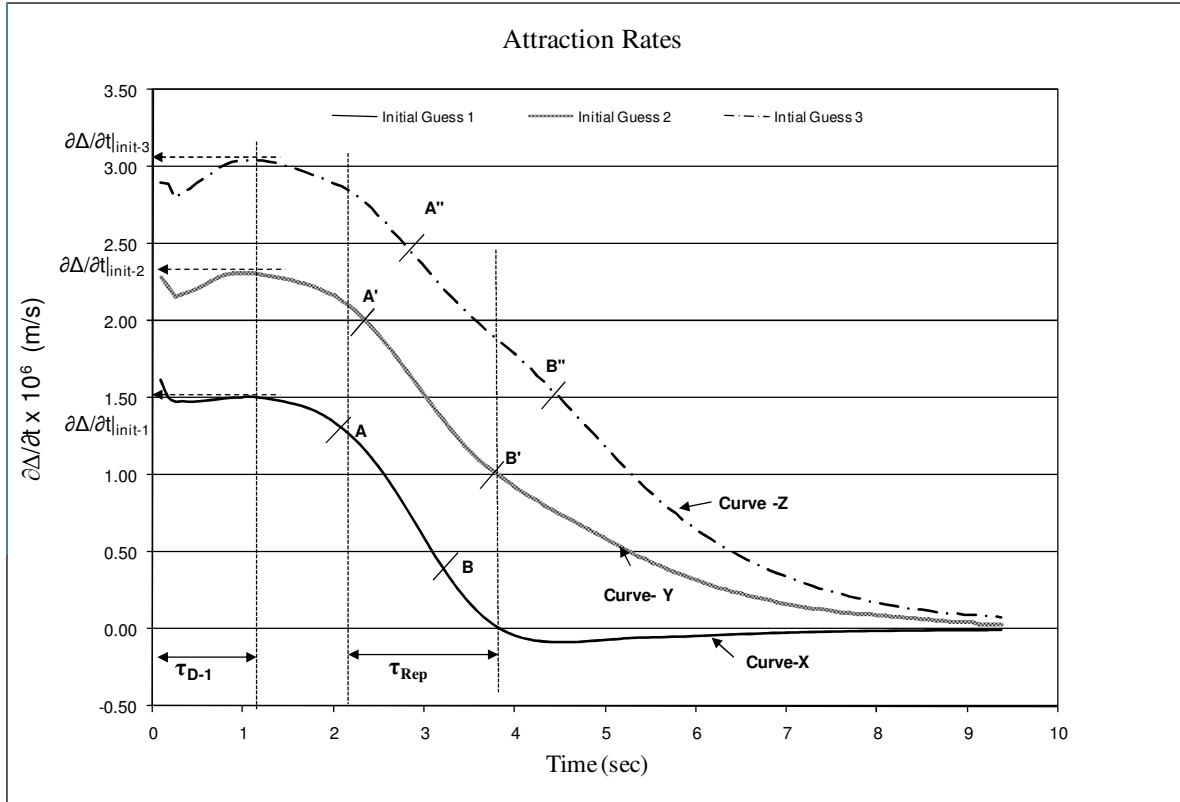


Fig. 11

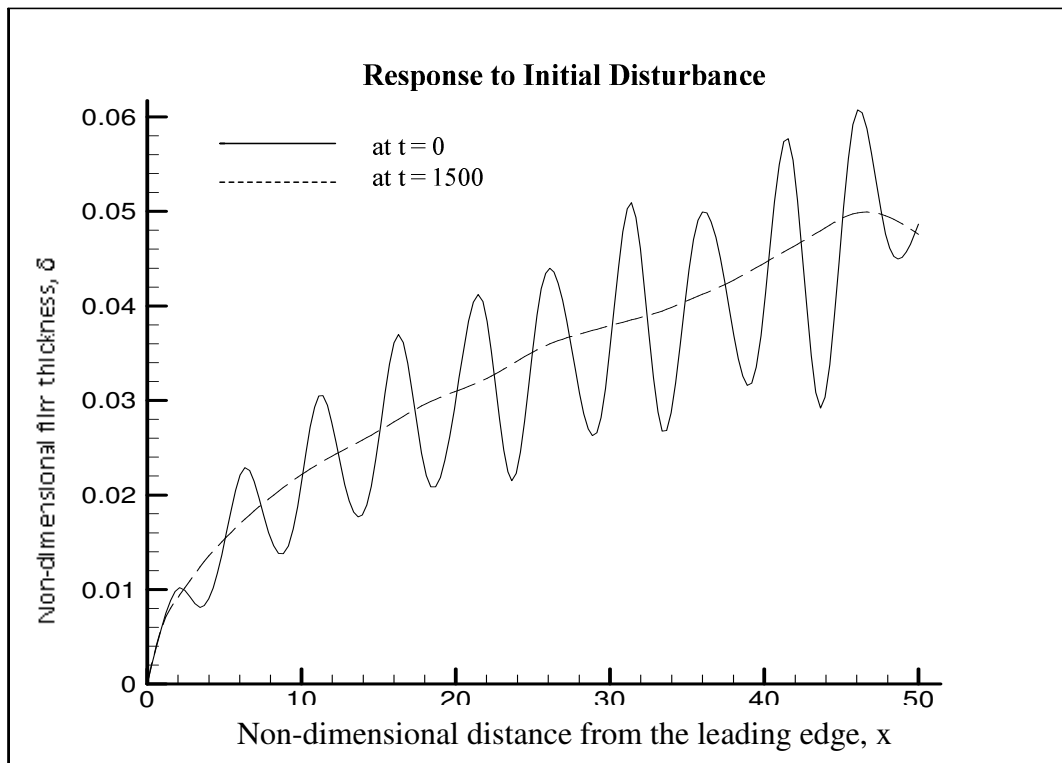


Fig. 12

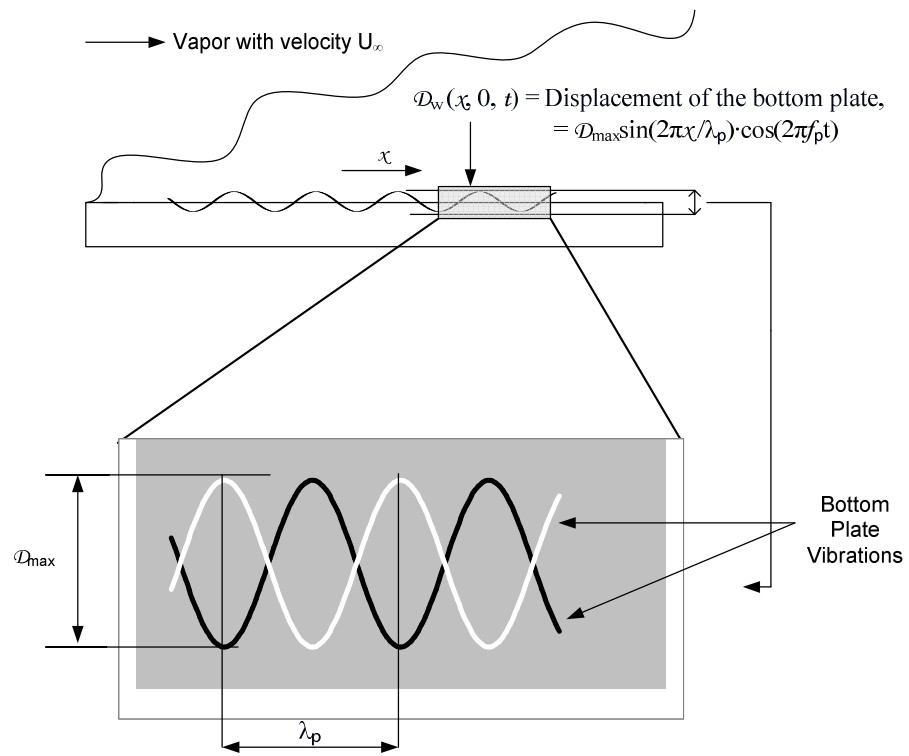


Fig. 13

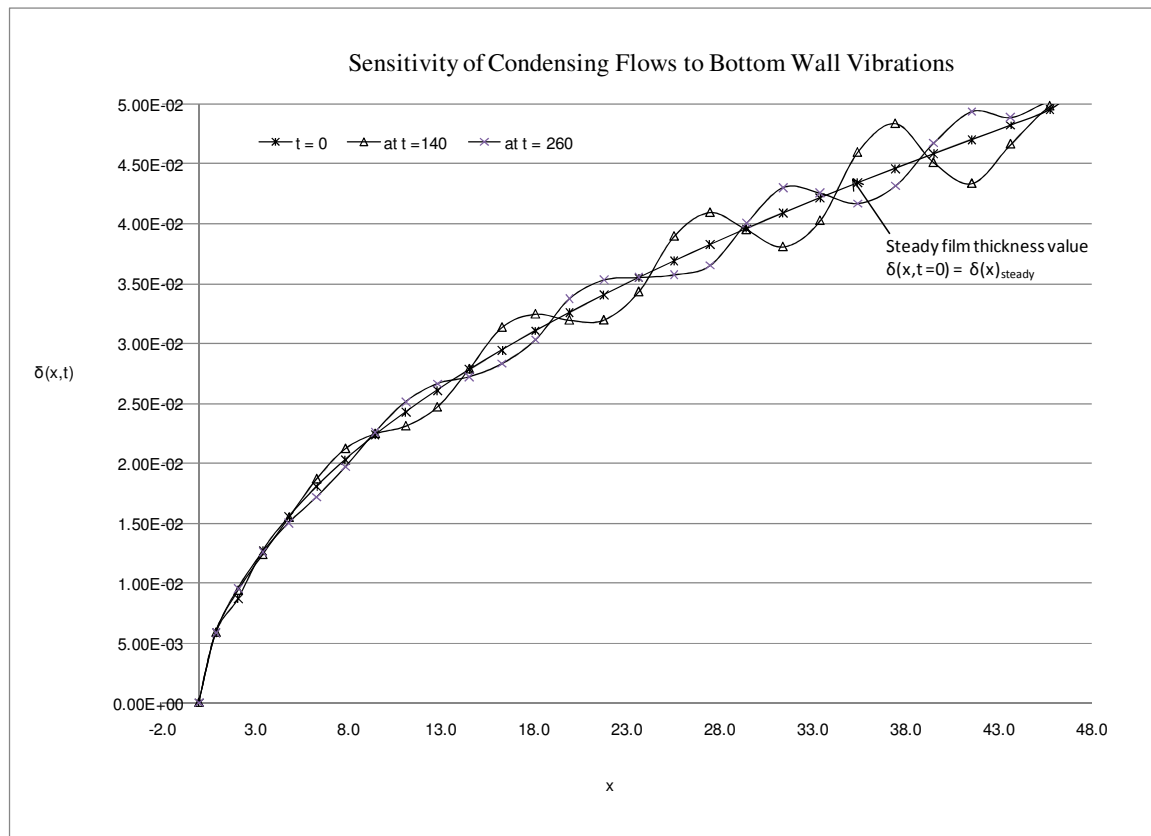


Fig. 14

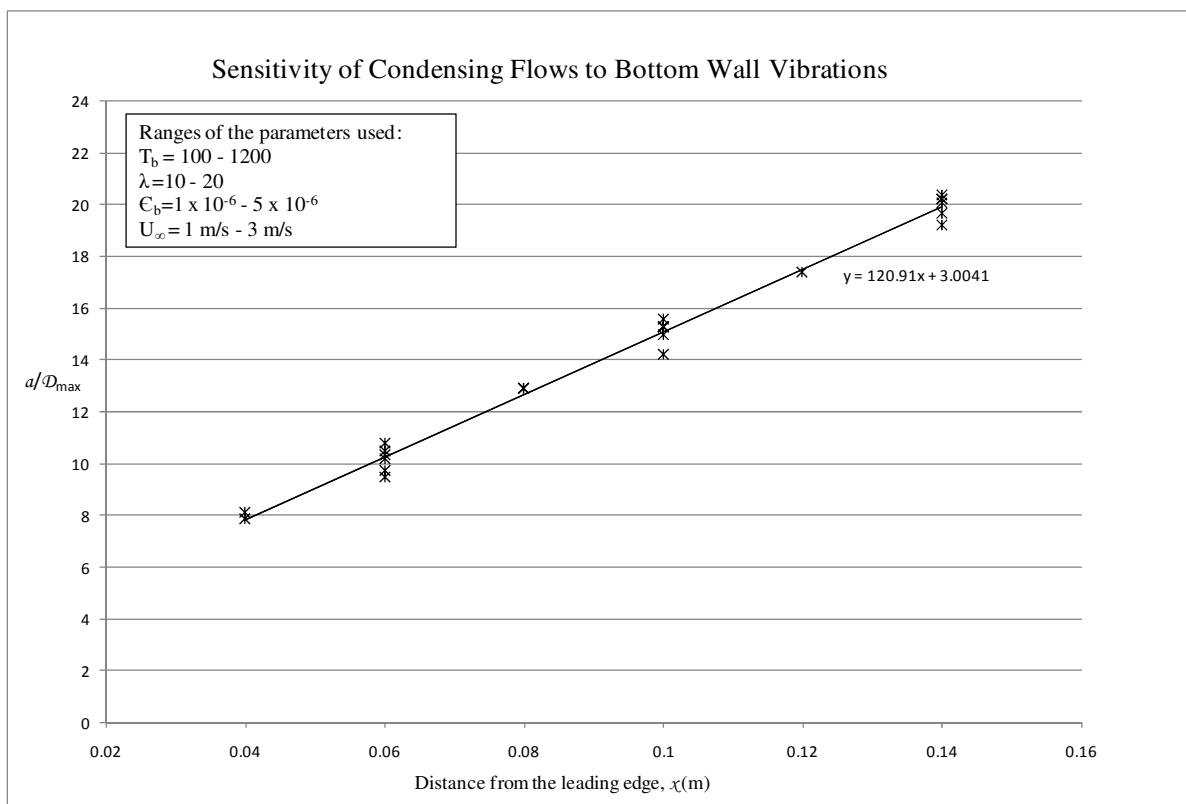


Fig. 15

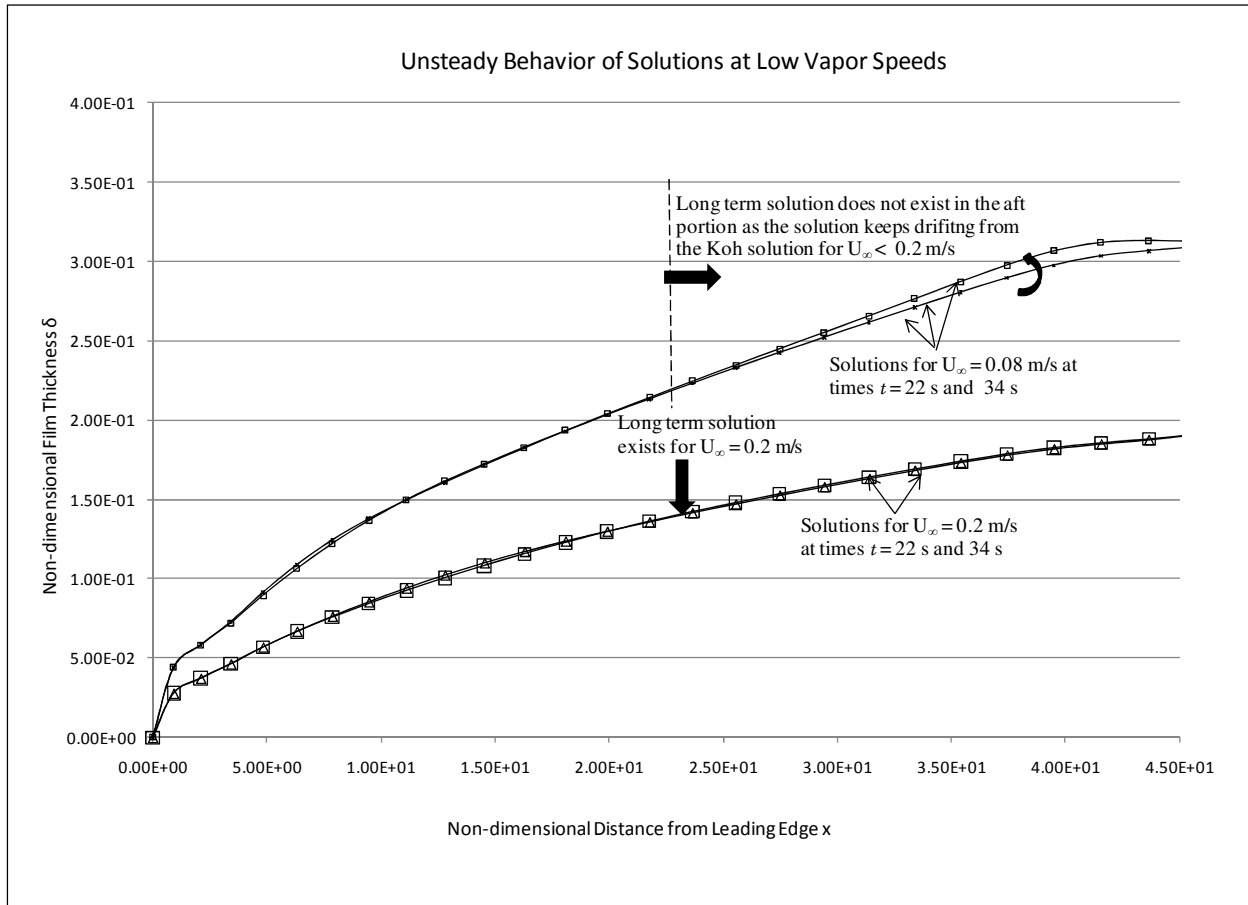


Fig. 16

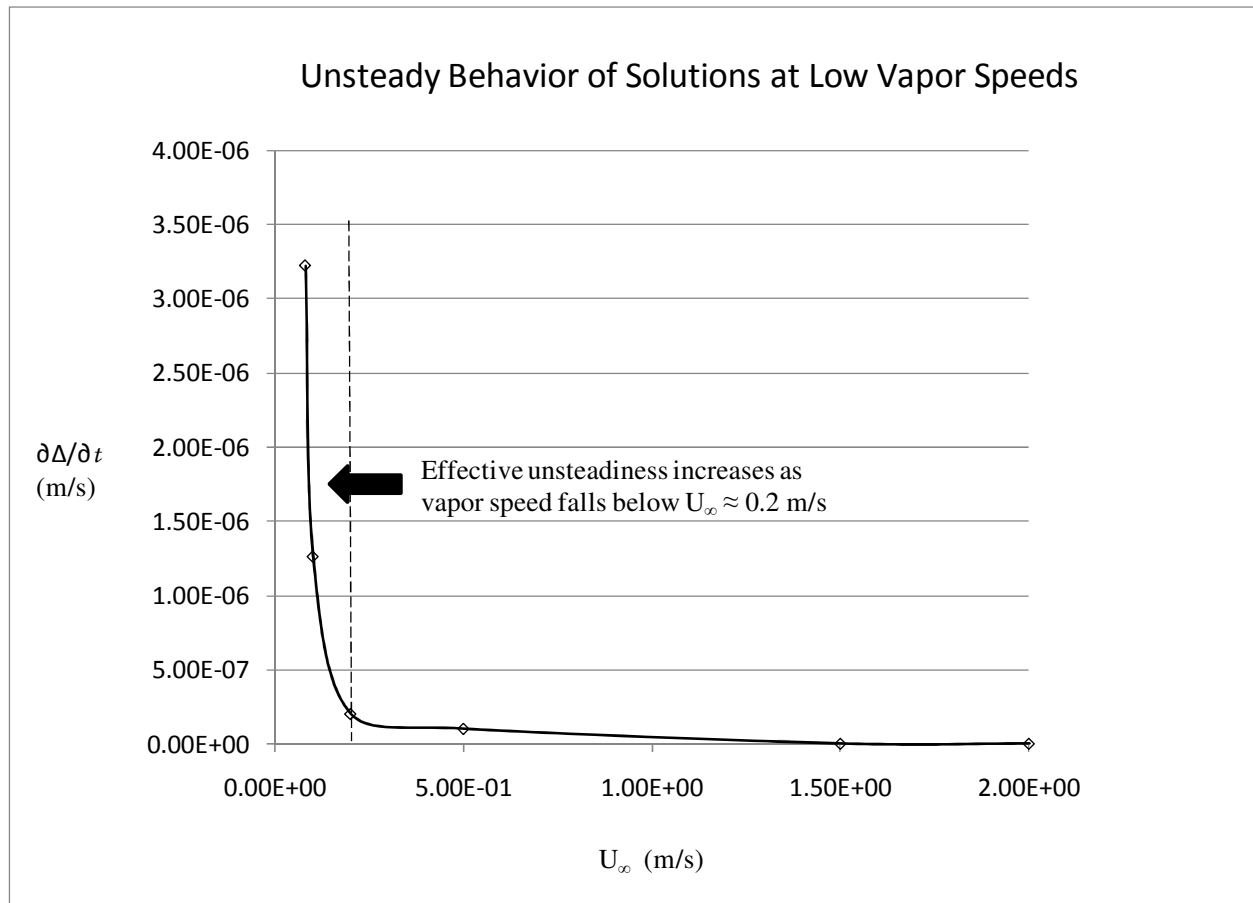


Fig. 17

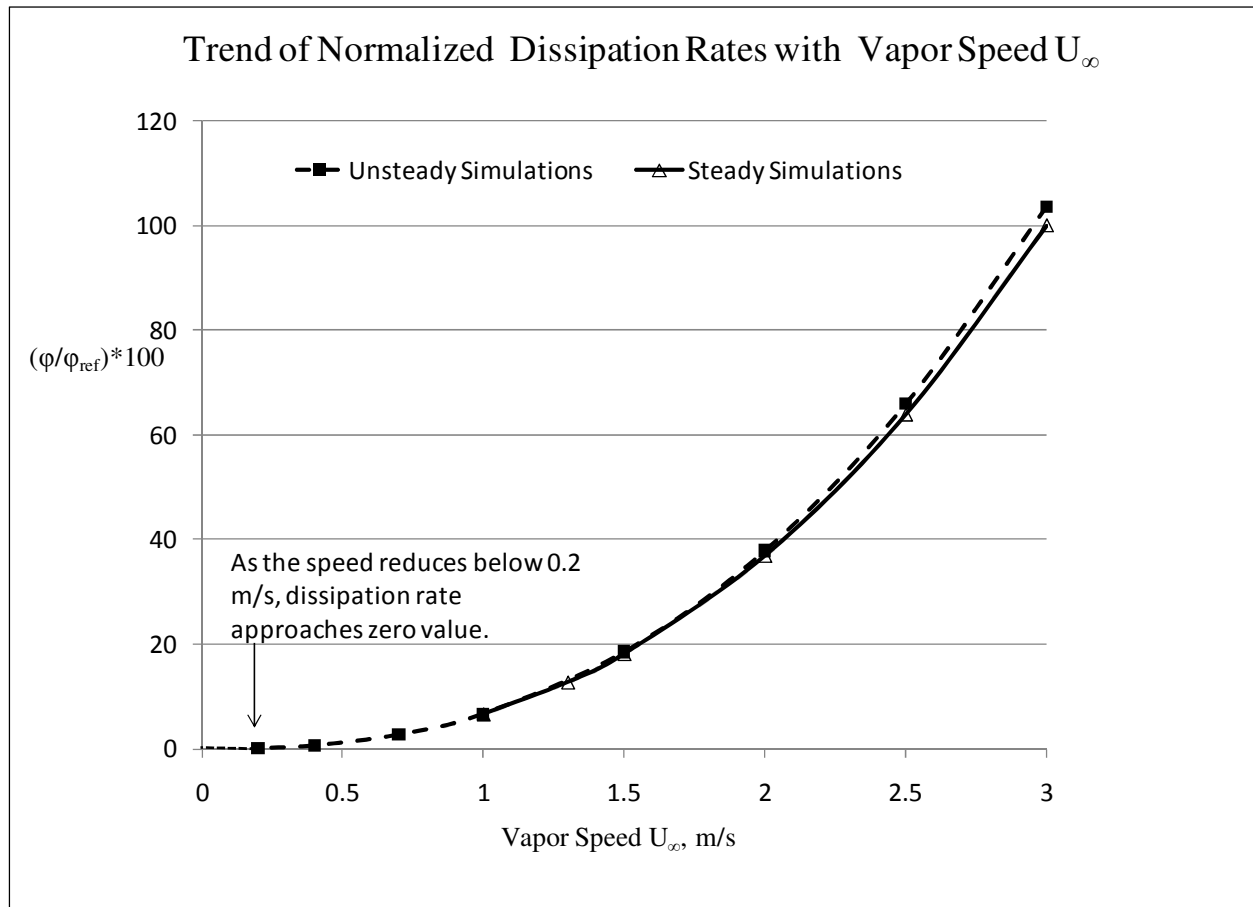


Fig. 18